*American Mineralogist, Volume 80, pages 776–798, 1995*

# Textures and Sr, Ba, Mg, Fe, K, and Ti compositional profiles in volcanic plagioclase: Clues to the dynamics of calc-alkaline magma chambers

**Bradley S. Singer, Michael A. Dungan**
Département de Minéralogie, Université de Genève, 13 rue des Maraîchers 1211, Genève 4, Switzerland
**Graham D. Layne**
Institute of Meteoritics, University of New Mexico, Albuquerque, New Mexico 87131, U.S.A.

## Abstract

Concentration profiles for Ca, Na, Al, K, Fe, Ti, Mg, Sr, and Ba obtained by electron microprobe and secondary ion mass spectrometry from plagioclase crystals, together with textural observations from interference contrast microscopy, are consistent with contrasting magma dynamics in two subvolcanic reservoirs from which silicic lavas erupted at the Tatara–San Pedro volcanic complex, Chilean Andes. The 1 $km^3$ late Pleistocene (68 ka) Tatara dacite is chemically homogeneous, phenocryst-poor, and contains crystals of opacitized hornblende, orthopyroxene, and titanomagnetite, plus 2 mm euhedral plagioclase phenocrysts with simple zoning patterns. Except at their rims, analyzed phenocrysts show nearly monotonic core-to-rim changes from $An_{52}$ to $An_{31}$, including slight decreases in MgO and FeO′ and slight increases in Ba, Sr, and K concentrations. Abrupt, but small, chemical shifts are associated with many subtle dissolution surfaces. In contrast, the 0.1 $km^3$ of chemically and texturally heterogeneous Holocene San Pedro dacite contains crystals of clinopyroxene, orthopyroxene, hornblende, biotite, titanomagnetite, ilmenite, and abundant 2 mm euhedral plagioclase phenocrysts, plus plagioclase and olivine xenocrysts derived from fragmented quenched basaltic inclusions. Analyzed phenocrysts span the range from $An_{72}$ to $An_{32}$. Abrupt increases of 15 mol% An, large increases in MgO, FeO′, and Sr, and decreases in Ba and $K_2O$ concentrations are associated with a few major dissolution surfaces. Plagioclase xenocrysts of $An_{74-86}$ have higher Sr, MgO, and FeO′ and lower Ba and K concentrations than the phenocrysts, reflecting crystallization from a basaltic melt. In both dacites, phenocryst rims decrease in Sr and increase in K and Ti relative to equilibrium values as a consequence of rapid crystal growth at high undercooling during magma ascent and eruption. Modeling of variations in apparent $D_{Sr}^{plag/melt}$ implies growth rates for the $\leq 100$ $\mu$m phenocryst rims of $10^{-9}$ cm/s, suggesting that magma ascent may have taken several months. Provided these kinetic effects are identified, the remainder of the concentration profiles for Sr, Ba, Mg, and K in plagioclase phenocrysts can be inverted using partition coefficient expressions to monitor the temporal evolution of melts in the preeruptive magma chambers.

Monotonic melt trends and periodic thermal dissolution of Tatara dacite phenocrysts imply a magma chamber closed to inputs of new magma and heat. Repeated cycles of crystal growth and weak dissolution occurred during phenocryst retention in thermally driven convection cells characterized by steady-state laminar flow. In contrast, dissolution events associated with large, abrupt shifts in melt Sr, Mg, and K/Ba toward basaltic values indicate that in the Holocene magma chamber heating of silicic melt adjacent to basaltic inclusions during magma mingling caused plagioclase dissolution. Renewed plagioclase growth from the resulting small volumes of hybrid melt recorded highly localized chemical mixing by diffusion and accompanying cycles of fractionation.

## Introduction

Processes in subvolcanic magma chambers play a major role in producing the spectrum of igneous rock compositions on Earth. Intrinsic phenomena include the following: cooling, crystallization, and convection of the magma, crystal fractionation or retention in residual melt, and chamberwide stratification (Hildreth, 1979; Marsh, 1989a; Druitt and Bacon, 1989). In addition, open-system behavior, including mechanical mingling, thermal equilibration, and chemical mixing of initially separate magmas (Eichelberger, 1978; Bacon, 1986), crustal assimilation (Wilcox, 1954; Bacon et al., 1989), and eruption and degassing (e.g., Rutherford and Hill, 1993; Cash-

0003–004X/95/0708–0776$02.00

man, 1992) are well documented. Despite theoretical and experimental studies focused on such processes (e.g., Sparks et al., 1984, 1993; Sparks and Marshall, 1986; Huppert and Sparks, 1988; Marsh, 1988, 1989a, 1989b; Weinstein et al., 1988; Oldenberg et al., 1989), extracting unambiguous information about the dynamic history of natural magmas has proved difficult (Marsh, 1990, 1991; Sparks, 1990; Huppert and Turner, 1991).

Plagioclase phenocrysts preserve records of the chemical and physical evolution of magma chambers (e.g., Anderson, 1984; Pearce et al., 1987; Blundy and Shimizu, 1991) because slow interdiffusion (Grove et al., 1984) ensures that their chemical and textural zoning reflects primary growth. The major element composition of plagioclase (albite-anorthite) and its stability are functions of intensive and kinetic parameters, including melt composition and $H_2O$ content, temperature and pressure (Tsuchiyama, 1985; Rutherford and Devine, 1988; Housh and Luhr, 1991), decompression (Nelson and Montana, 1992), and growth rate (Lofgren, 1980). Thus, it is difficult to discriminate uniquely among rival magmatic effects on the basis of binary compositional variations. Since Homma's (1932) interpretation that oscillatory zoned plagioclase in andesitic lavas recorded thermally driven magmatic convection cycles, many petrologists have sought to correlate zoning in plagioclase with specific magmatic processes.

An approach that can be used in conjunction with profiles of binary plagioclase components is to examine variations in nonbinary components present at minor (<5000 ppm) or trace (<500 ppm) levels in these phenocrysts. Depending on the element, these concentrations reflect abundances in the melt, An content of the plagioclase, and kinetic factors such as diffusion in the melt and crystal growth rates. In this paper we address the behavior of nonbinary elements present at variable concentrations in coexisting melts, including the major elements Mg, Fe, Ti, and K. The elements Sr and Ba, which are present in trace amounts in the liquid but at minor (Sr) or trace (Ba) concentrations in plagioclase, are presumed (along with K) to occur as stoichiometric nonbinary feldspar substitutions.

The precisions of Sr, Ba, Mg, and Fe determinations in plagioclase by EPMA are limited by low count rates, high detection limits, Na volatilization, and Fe fluorescence (e.g., Longhi et al., 1976). Druitt and Bacon (1989) discriminate between high-Sr (>2500 ppm) and low-Sr (<1500 ppm) plagioclase phenocrysts with a $2\sigma$ precision of ±20% (300–500 ppm). Such uncertainties preclude application of EPMA data to studies of zoning in which the goal is to quantify subtle compositional variations in liquids or to separate kinetic from compositional and thermal effects. Secondary ion mass spectrometry (SIMS) using an ion microprobe permits more precise measurements of nonbinary element concentrations in plagioclase (Meyer et al., 1974; Steele et al., 1980). The ion probe provides the spatial resolution ($\leq 10$ $\mu$m) and analytical precision (±2–5%) necessary for inversion of zoning profiles for elements such as Sr, Mg, and Ba to obtain records of melt evolution (Meyer et al., 1974; Shimizu, 1978; Blundy and Shimizu, 1991).

Compositionally dependent textural features in etched plagioclase crystals may be imaged at the micrometer scale using reflected-light Nomarski differential interference contrast (NDIC) microscopy (Anderson, 1983). Internal features of plagioclase phenocrysts, such as dissolution surfaces and fine oscillatory growth zoning, which are difficult to detect in transmitted light, are readily visible with NDIC (Pearce et al., 1987; Pearce and Kolisnik, 1990). All EPMA and SIMS data in this study were obtained following thorough documentation of dissolution and growth features using NDIC imagery.

Calculations of transient melt compositions from solid-phase compositions require partitioning expressions that accurately incorporate thermal and compositional dependencies. The types of dependencies inherent in plagioclase-melt expressions differ for Sr, Ba, Fe, Mg, and K (Blundy and Wood, 1991; Longhi et al., 1976; Nagasawa and Schnetzler, 1971). Although errors in these expressions (analytical and formulaic) apparently do not preclude the applications proposed in this paper, additional determinations on the basis of carefully designed experiments could resolve several outstanding questions (Morse, 1992; Blundy and Wood, 1992, 1994). The $D_{Sr}^{plag/melt}$ and $D_{Ba}^{plag/melt}$ relations derived by Blundy and Wood (1991) from experimental data are based on their conclusion that partitioning of Sr and Ba between plagioclase and melt is insensitive to melt composition and temperature and is principally a function of An content of the crystal. This interpretation is reinforced by experiments illustrating relations between cation charge and radius, lattice site energetics, and partition coefficients (Blundy and Wood, 1994). Experiments of Longhi et al. (1976) also suggest that partition coefficients for Mg and Fe in plagioclase are largely independent of melt composition. Thus, if crystal growth occurred under near-equilibrium conditions, measurements of Sr, Ba, Mg, and Fe concentrations in plagioclase permit calculations of concentrations in the coexisting melt.

Melt compositions calculated in this manner must be viewed with caution because high rates of crystal growth at large undercoolings may induce significant departures from equilibrium (Albarede and Bottinga, 1972; Shimizu, 1983). Blundy and Shimizu (1991) argued that plagioclase growth rates in plutons are sufficiently low as to preclude departure from equilibrium. Our results demonstrate that this assumption is not always valid for volcanic rocks. The role of kinetics in minor and trace element partitioning needs careful investigation. Moreover, the thermal and chemical histories of different parts of magma chambers are different, and where convective motions occur, phenocrysts with different histories will be brought into close proximity.

The goals of this study are twofold: (1) to demonstrate the efficacy of integrated NDIC-EPMA-SIMS studies in resolving temporal records of magma evolution and crys-

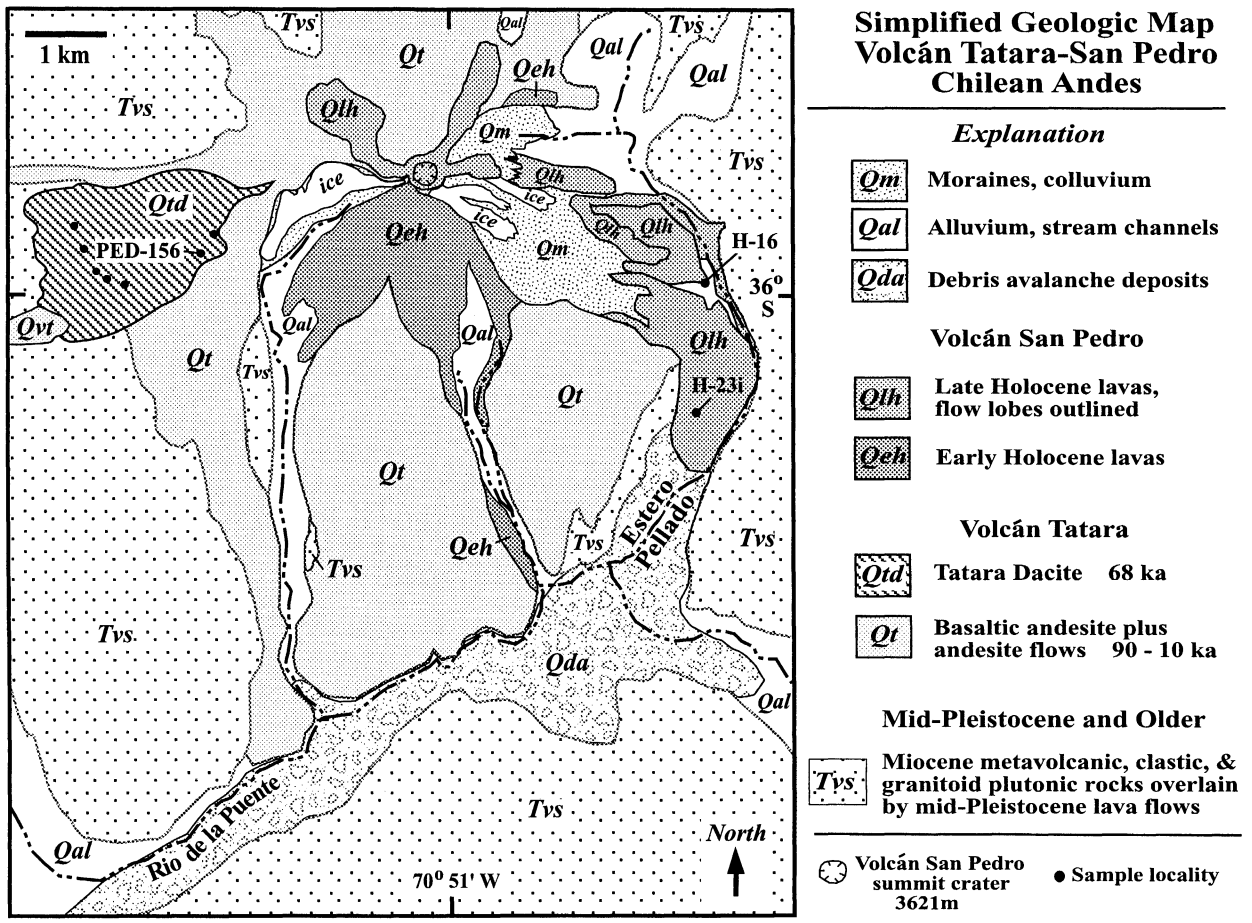


Fig. 1. Simplified geologic map of Volcán Tatara–San Pedro, Chilean Andes. Locations of dacitic lava samples PED-156 and H-16 and the quenched basaltic inclusion H-23i in the Holocene lava flow are given.

tallization from zoned plagioclase phenocrysts, and (2) to show from contrasting plagioclase zoning patterns that the compositional evolution, convective regimes, and cooling histories of dacitic magmas stored in chambers below arc volcanoes can vary considerably over short (~60 ka) time intervals. Phenocrysts from two dacitic lavas erupted at Volcán Tatara–San Pedro in the Chilean Andes were studied. These dacites were chosen because there are many independent indications that the reservoirs from which these magmas erupted were different. Specifically, the older dacite displays virtually no evidence of heterogeneity or open-system evolution, whereas the younger is part of a strongly zoned eruption that includes basaltic and silicic components (Singer and Dungan, 1992). Thus, observations derived from the study of a few carefully chosen plagioclase crystals are interpreted on the basis of abundant contextual information. The difficulties of extrapolation from representative phenocrysts to generalizations about chamberwide phenomena are also discussed.

## Dacitic lavas at Volcán Tatara-San Pedro

Volcán Tatara–San Pedro is the youngest edifice in the composite 75 km³ Tatara–San Pedro volcanic complex in the Andean Southern Volcanic Zone of Chile (Fig. 1; Ferguson et al., 1992). Volcán Tatara comprises 22 km³ of mainly basaltic andesitic lava flows with 52–56% $SiO_2$, erupted between 90 and 20 ka (Singer et al., 1994). The most voluminous single lava flow is, however, the 1 km³ Tatara dacite that erupted at 68 ± 6 ka from high on the western flank of the volcano (Fig. 1; Ferguson et al., 1992). No tephra deposits have been found in association with this nonvesicular dacitic lava; it is phenocryst-poor, containing ~8% plagioclase phenocrysts (0.5–2.5 mm) of $An_{31-52}$, ~0.5% microphenocrysts (<0.1 mm) of orthopyroxene, 0–1.5% hornblende phenocrysts (<0.5 mm) with opaque rims, and ~0.1% titanomagnetite phenocrysts in a fine-grained plagioclase-dominated holocrystalline matrix (Table 1; Fig. 2A). On the basis of four major and trace element analyses of bulk samples and petrographic examination of 15 thin sections (Fig. 1), the Tatara dacite is remarkably uniform in composition. Textural and mineralogical heterogeneity is minimal; the main variant occurs as ~300 m² patches of the flow lacking hornblende. This probably reflects a preeruptive $H_2O$ pressure and temperature close to the stability limit of amphibole, and possibly amphibole resorption during magma ascent and degassing (Rutherford and Hill, 1993).

**TABLE 1.** Compositions, mineral modes, and rheological properties of Tatara–San Pedro materials

| Sample | Tatara dacite Ped-156 | San Pedro dacite H-16 | San Pedro matrix glass* | San Pedro glass incl. | San Pedro basalt incl. H-23i |
|---|---|---|---|---|---|
| $SiO_2$ | 67.4 | 65.8 | 73.4 | 73.5 | 52.4 |
| $TiO_2$ | 0.47 | 0.51 | 0.38 | 0.16 | 0.99 |
| $Al_2O_3$ | 16.4 | 16.3 | 14.3 | 13.5 | 17.2 |
| $Fe_2O_3$ | 3.36 | 4.16 | 1.12 | 1.88 | 9.42 |
| MnO | 0.12 | 0.08 | 0.05 | 0.04 | 0.15 |
| MgO | 0.84 | 1.78 | 0.12 | 0.10 | 7.42 |
| CaO | 2.67 | 4.08 | 1.31 | 1.16 | 8.07 |
| $Na_2O$ | 5.07 | 4.54 | 3.81 | 2.23 | 3.27 |
| $K_2O$ | 2.78 | 2.70 | 3.85 | 3.93 | 1.09 |
| $P_2O_5$ | 0.17 | 0.16 | — | — | 0.22 |
| Total | 99.2 | 100.0 | 98.3 | 96.6 | 100.3 |
| Sr | 382 | 452 | | | 564 |
| Ba | 561 | 618 | | | 330 |
| | | **Modes**** | | | |
| Plagioclase | 8.0 | 15.3 | | | 46.1 |
| Clinopyroxene | — | 0.7 | | | 6.2 |
| Orthopyroxene | 0.5 | 0.5 | | | 2.1 |
| Hornblende | 1.5 | 3.8 | | | 3.7 |
| Biotite | — | 0.3 | | | — |
| Magnetite | 0.1 | 1.2 | | | 2.8 |
| Olivine | — | 0.1 | | | 10.2 |
| Σ crystals | 10.1 | 21.9 | | | 71.2 |
| | | **Properties†** | | | |
| $T$ (°C) | 900 | 950 | 950 | | 1150 |
| $H_2O$ (wt%) | 2.0 | 2.0 | 2.0 | | 1.0 |
| $\rho$ magma (g/cm³) | 2.23 | 2.27 | 2.17 | | 2.55 |
| $\rho$ plagioclase‡ | 2.62 | 2.64 | 2.64 | | 2.69 |
| log $\mu_L$ poise | 5.8 | 5.4 | 6.6 | | 2.9 |
| log $\mu_c$ poise | 6.0 | 5.9 | 7.1 | | infinite |
| log $V_s$ (m/s) | −6.3 | −7.0 | −8.1 | | |
| log $V_c$ (m/s) | −6.6 | −7.4 | −8.5 | | |

*Note:* oxides in weight percent, Sr and Ba in parts per million, mineral modes in volume percent. Dacite and inclusion analyses by XRF at University of Massachusetts.

* Means of seven electron probe analyses.

** Volume percent crystals > 0.03 mm.

† Calculations described in Appendix 1.

‡ Assumes Tatara magma with $An_{40}$, San Pedro dacite with $An_{60}$, and basaltic inclusion with $An_{80}$.

The Tatara dacite plagioclase phenocrysts analyzed here are in one polished thin section of sample PED-156 (Figs. 1, 2A, and 3A; Table 1; Ferguson et al., 1992).

In contrast to the relatively homogeneous Tatara dacite, the San Pedro dacite (Fig. 1; Table 1) is the earliest 0.1 km³ lava lobe in a late Holocene eruption of 1 km³ of chemically, mineralogically, and thermally zoned magma (Ferguson et al., 1992; Singer and Dungan, 1992). Late Holocene tephra deposits indicate that an initial explosive phase was followed by extrusion of nonvesicular dacitic lava. These eruptions were preceded by a 5 km³ sector collapse-debris avalanche created by structural failure of the southeast flank of Volcán San Pedro (Fig. 1). Inferred deeper levels of the stratified magma chamber contained two-pyroxene dacite (0.85 km³) and lesser andesite (0.05 km³). The two-pyroxene dacite contains up to 5 vol% of 1–30 cm diameter inclusions of quenched glass-rich basalt containing phenocrysts of plagioclase, olivine, clinopyroxene, orthopyroxene, titanomagnetite, and interstitial microphenocrysts of amphibole (Table 1). Similar inclusions, up to several centimeters in diameter, occur in the San Pedro dacite (Fig. 2C). The San Pedro dacite sample (H-16; Fig. 1; Table 1) contains ~22% phenocrysts, including two populations of plagioclase (15%) and $Fo_{70-81}$ olivine crystals (0.1%), plus phenocrysts of clinopyroxene (0.7%), orthopyroxene (0.5%), biotite (0.3%), titanomagnetite (1.2%), and euhedral hornblende lacking opacite rims (3.8%), in a rhyolitic glass matrix (Singer and Dungan, 1992; Table 1; Fig. 2B and 2C). Of the two plagioclase populations, the more abundant comprises strongly zoned crystals of $An_{72-32}$. A less abundant population has distinctive anhedral cores with a micrometer-scale sieve-texture (Fig. 2B and 2C); the cores and most rims are $An_{75-85}$. Textural and compositional similarities suggest that the sieve-cored plagioclase and magnesian olivines are xenocrysts derived from mechanical fragmentation and dispersion of the basaltic inclusions (Fig. 2C; Table 1) into the dacitic magma (Singer and Dungan, 1992).

## ANALYTICAL METHODS

Polished thin sections from the two dacite samples were etched for 60–120 s in concentrated $HBF_4$ prior to EPMA and SIMS analyses to create microtopographic (±0.25 μm) relief for NDIC microscopy. EPMA measurements of plagioclase were obtained with a JEOL 733 instrument utilizing a 15 kV potential, 15 nA sample current, and 5 μm diameter beam to minimize Na loss. Glass inclusions in plagioclase and matrix glass were analyzed with a 7.5 nA current and a defocused 10 μm beam. From repeated

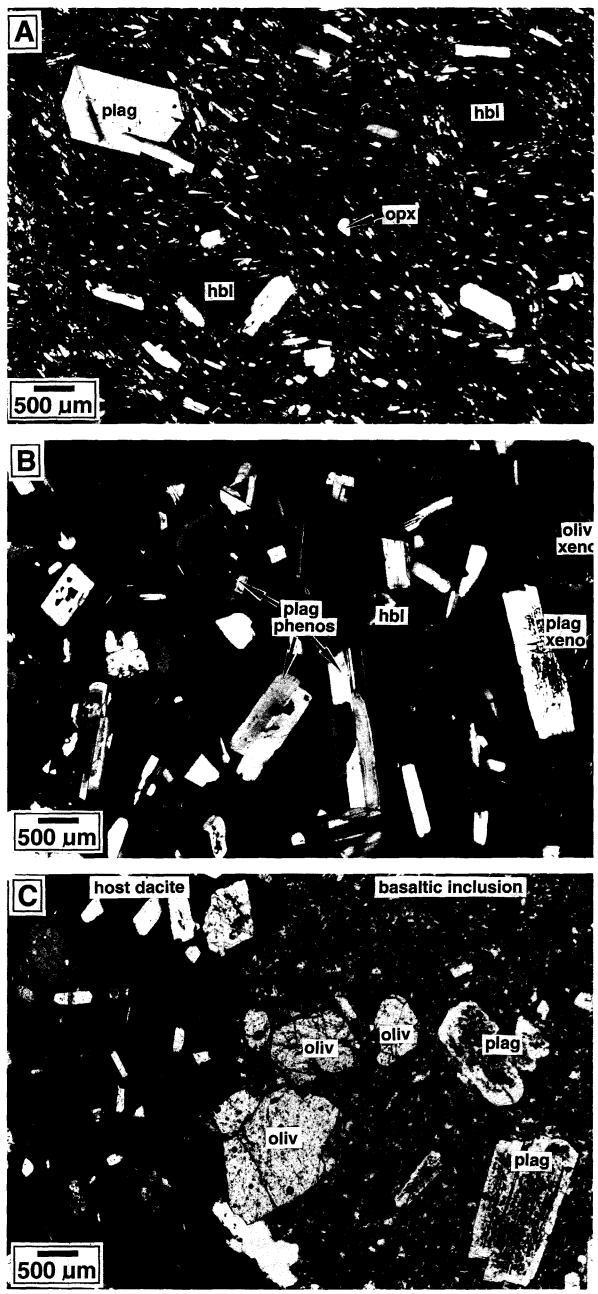


Fig. 2. Photomicrographs of textures and minerals. (**A**) Tatara dacite. Sparse plagioclase phenocrysts and hornblende with thin opacitized rims in a holocrystalline groundmass with abundant plagioclase microlites (transmitted light, crossed polars). (**B**) San Pedro dacite. Phenocrysts of plagioclase and unrimmed hornblende plus xenocrysts of plagioclase and olivine (rimmed by opx) in a rhyolitic glass matrix (transmitted light, crossed polars). (**C**) San Pedro dacite with <2 cm basaltic inclusion. Note the distinctive sieve cores of plagioclase crystals in the inclusion (transmitted light). Plag = plagioclase, hbl = hornblende, oliv = olivine.

measurements of natural and synthetic feldspar standards, precisions for CaO, $Na_2O$, $K_2O$, FeO′, and $SiO_2$ are estimated at ~2–3%. Concentrations were calculated using Bence-Albee corrections. Representative crystals in each of the two sections were chosen for EPMA traverses from which >4000 major element analyses were obtained along core-to-rim traverses in 28 crystals. On the basis of major element profiles and textural features, three typical crystals, including one phenocryst from each dacite and a xenocryst from the San Pedro dacite, were chosen for SIMS measurements, which were made along core-to-rim traverses adjacent to the EPMA traverses.

SIMS analyses were obtained using a CAMECA IMS 4f ion microprobe. Samples were bombarded with $O^-$ ions accelerated through a nominal potential of 10 kV. Energy filtering (Shimizu, 1978) using a high-voltage offset of −105 V and an energy window of 50 V effectively eliminated isobaric interferences. Sputtered positive secondary ions were thus extracted from the sample through a potential of 4395 V. Each spot was pre-prepared for 2–3 min by bombardment with a 25 μm rastered primary beam to clean away surface contamination. A 1–2 nA primary beam was then focused to a 10 μm diameter analytical spot. After an additional 1 min wait to allow the sputtering crater to reach steady state, peak signals for $^{23}Na^+$, $^{24}Mg^+$, $^{27}Al^+$, $^{28}Si^+$, $^{41}K^+$, $^{40}Ca^+$, $^{47}Ti^+$, $^{56}Fe^+$, $^{88}Sr^+$, and $^{138}Ba^+$ were counted cyclically for approximately 15 min. Concentrations were obtained by comparison of the measured ratios of the peaks to that of $^{28}Si^+$ and by normalization to $SiO_2$, with replicate determinations of the same ratios in a standard grain of Lake County plagioclase. We used the following values (Mg, Sr, Ba, Ti by isotope dilution from Meyer et al., 1974; others by EPMA from M. Spilde, personal communication) for this standard: $SiO_2$ (51.7 wt%), $Al_2O_3$ (30.1%), CaO (13.2%), $Na_2O$ (3.82%), K (913 ppm), Fe (3032 ppm), Mg (820 ppm), Sr (582 ppm), Ba (63 ppm), and Ti (228 ppm).

Internal precision (mean deviation of peak counting cycles) for each spot analysis is typically better than 0.5% for Al, 1.0% for Na and Ca, 1.5% for Fe and Sr, 2.0% for K and Ba, 2.5% for Mg, and 3.5% for Ti. These variations reflect counting statistics, instrument variations, and the submicrometer heterogeneity of the volume analyzed in each spot. As such they are the most appropriate measure of precision for intercomparison of the plagioclase analyses presented here. An additional uncertainty is present in the absolute values calculated for each element because of substantial small-scale heterogeneity of some elements in the standard plagioclase. On the basis of replicate analyses of the standard made during each analytical session, this uncertainty should not exceed 1.0% Al, 2.0% Na, 2.5% Mg, 3.5% Ca, 4.0% Ti, 4.5% Fe, 5.5% Sr, 6.5% Ba, and 7% K of the elemental concentrations. The mole percent anorthite for each spot was calculated from the ratio Ca/(Ca + Na + K); anorthite contents calculated in this manner agree within 2–3% (absolute) of the nearby EPMA analyses.

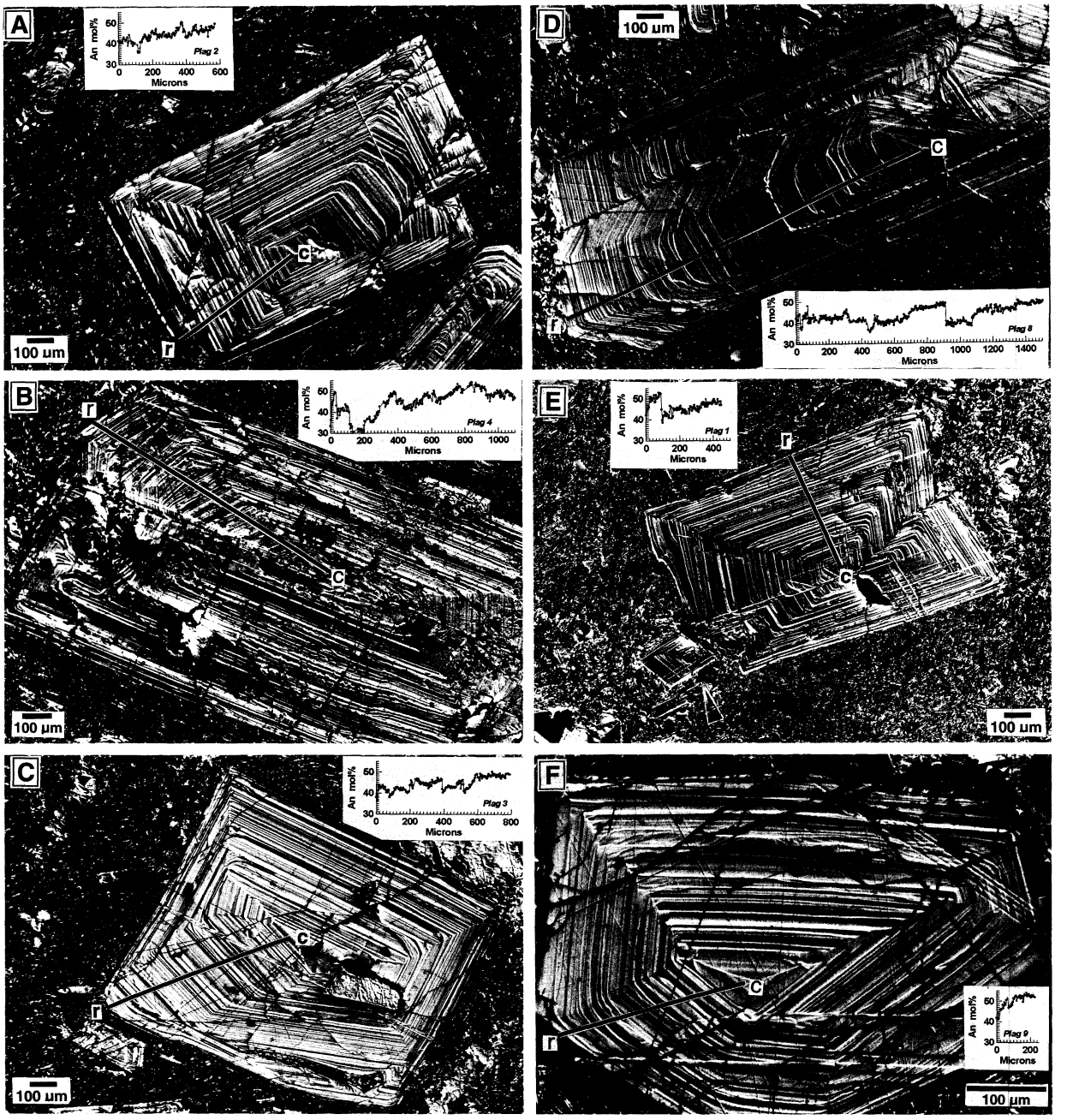


Fig. 3. NDIC images and EPMA profiles of An content vs. distance from the rim (micrometers) for six plagioclase phenocrysts in Tatara dacite sample PED-156. Note that the scale of the An profiles does not match those of the photomicrographs. Cores (c) and rims (r) of the EPMA profiles are marked on the images. In each phenocryst (**A-F**), many euhedral oscillatory zones are slightly truncated by several subtle dissolution surfaces. All crystals are sector zoned except in **D**. An profiles show small abrupt shifts at the dissolution surfaces. Within their outermost 50 $\mu$m, phenocrysts in **A**, **B**, **C**, **D**, and **F** contain intervals at reverse zoning.

## Plagioclase morphology and electron probe analyses

Textural observations are critical to interpretations of plagioclase zoning (e.g., Pearce and Kolisnik, 1990; Singer et al., 1993). Accordingly, in this section the textural features of plagioclase in the two dacites are highlighted, and the corresponding EPMA profiles are described with respect to these observations.

### Tatara dacite

Tatara dacite phenocrysts are sector-zoned, equant euhedra, 0.5–2.5 mm across. The prevailing pattern in

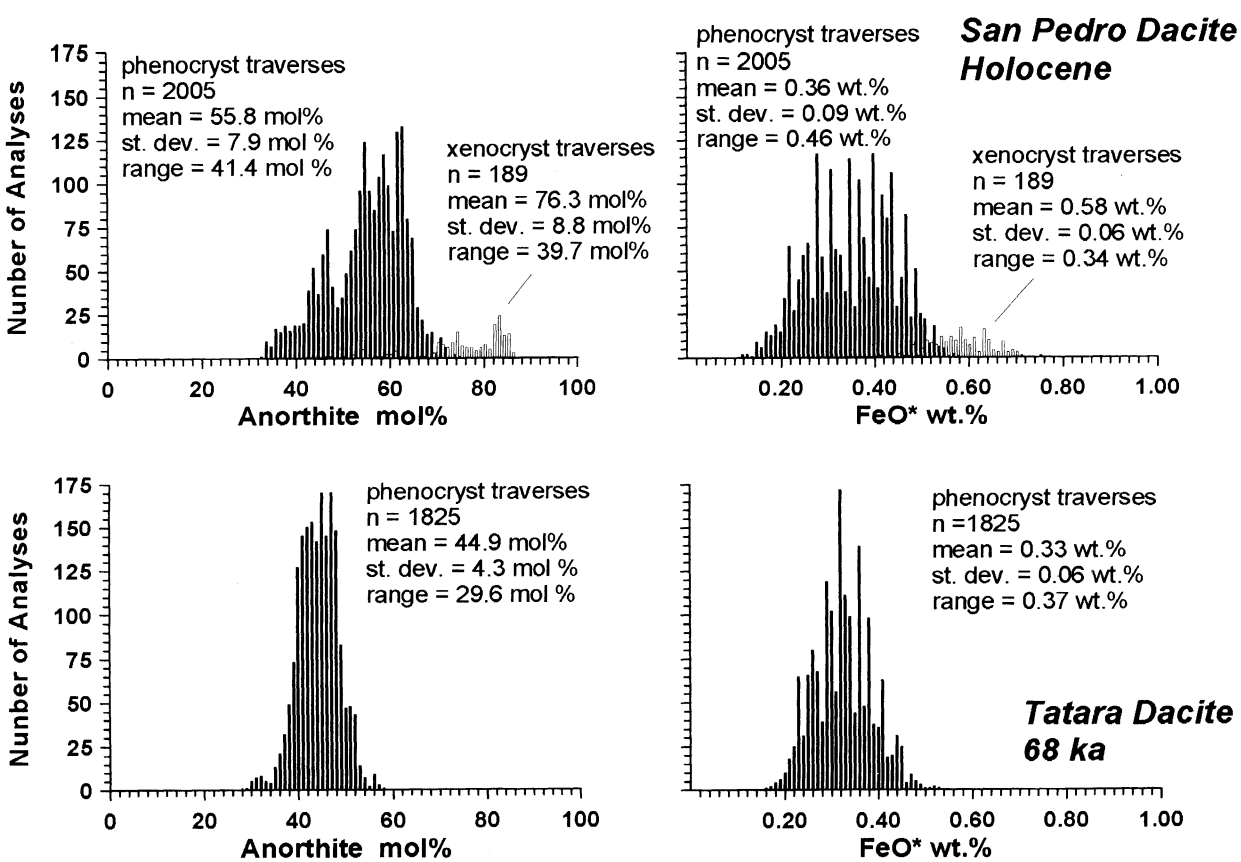


Fig. 4. Histograms summarizing >4000 EPMA measurements of plagioclase crystals in the Tatara (lower) and San Pedro (upper) dacites. Phenocrysts in dark fill, xenocrysts hollow pattern. The San Pedro dacite phenocrysts have a broader range in An content, are generally more calcic, and have higher FeO′ than the Tatara phenocrysts. The San Pedro dacite contains calcic Fe-rich xenocrysts as well.

EPMA profiles is a gradual decrease in An content from cores of $An_{45-50}$ to rims of $An_{36-42}$ (Fig. 3). Superimposed on this trend are: (1) dozens of planar oscillatory zones 1–5 μm thick; a typical crystal 1.5 mm across may have >100 fine-scale oscillatory zones from core to rim (Fig. 3); and (2) many subtle dissolution surfaces where underlying planar zones are truncated (Fig. 3). Plagioclase overgrown on these surfaces is always more An rich (but typically <5 mol% An) than the underlying plagioclase. Rarely, abrupt shifts of ~10 mol% are present (Fig. 3C). In addition, several of the analyzed crystals are reversely zoned within the interval 50–75 μm from the rim, but all are normally zoned in the outermost 50 μm. The complete population of EMPA analyses defines frequency maxima with restricted ranges of $An_{44\pm14}$ and 0.33 ± 0.18 wt% FeO′ (Fig. 4).

### San Pedro dacite

Phenocrysts in the San Pedro dacite are generally euhedral and 0.5–2.0 mm across. Their internal textures and compositions, however, differ considerably from phenocrysts in the Tatara dacite. These differences include: (1) zoning from more calcic cores ($An_{65}$) to more sodic rims ($An_{32}$) (Fig. 5), (2) major dissolution surfaces with irregular but sharp boundaries across which there are abrupt rimward shifts to 10–20 mol% higher An contents, and (3) broad frequency distributions with ranges of $An_{53\pm21}$ and 0.36 ± 0.29 wt% FeO′ (Fig. 4). Moreover, there are fewer well-defined 1–5 μm euhedral oscillatory zones. Where oscillatory zoning is weak or nearly absent, steep normally zoned compositional gradients occur. The 100+ μm intervals of steep normal zoning are frequently terminated at dissolution surfaces that truncate dozens of underlying planar zones. In some crystals, 10 × 30 μm inclusions of rhyolitic glass, nearly identical to the matrix glass (Table 1; Figs. 5 and 6B), are trapped in sodic plagioclase along major dissolution surfaces.

The San Pedro dacite also contains 2–3% euhedral tabular, 1–2 mm long plagioclase xenocrysts (Figs. 2B, 2C, and 5C). All have anhedral micrometer-scale sieve-textured cores with mineral and glass inclusions occupying interstices. Anhedral cores are overgrown by ~100–200 μm thick mantles that consist of euhedral oscillatory zones 1–5 μm thick. The xenocrysts are nearly unzoned; most have $An_{80-83}$ cores and mantles. A few are normally zoned in the outermost 20–30 μm. Xenocrysts are distinguished from the phenocrysts not only by morphology and An

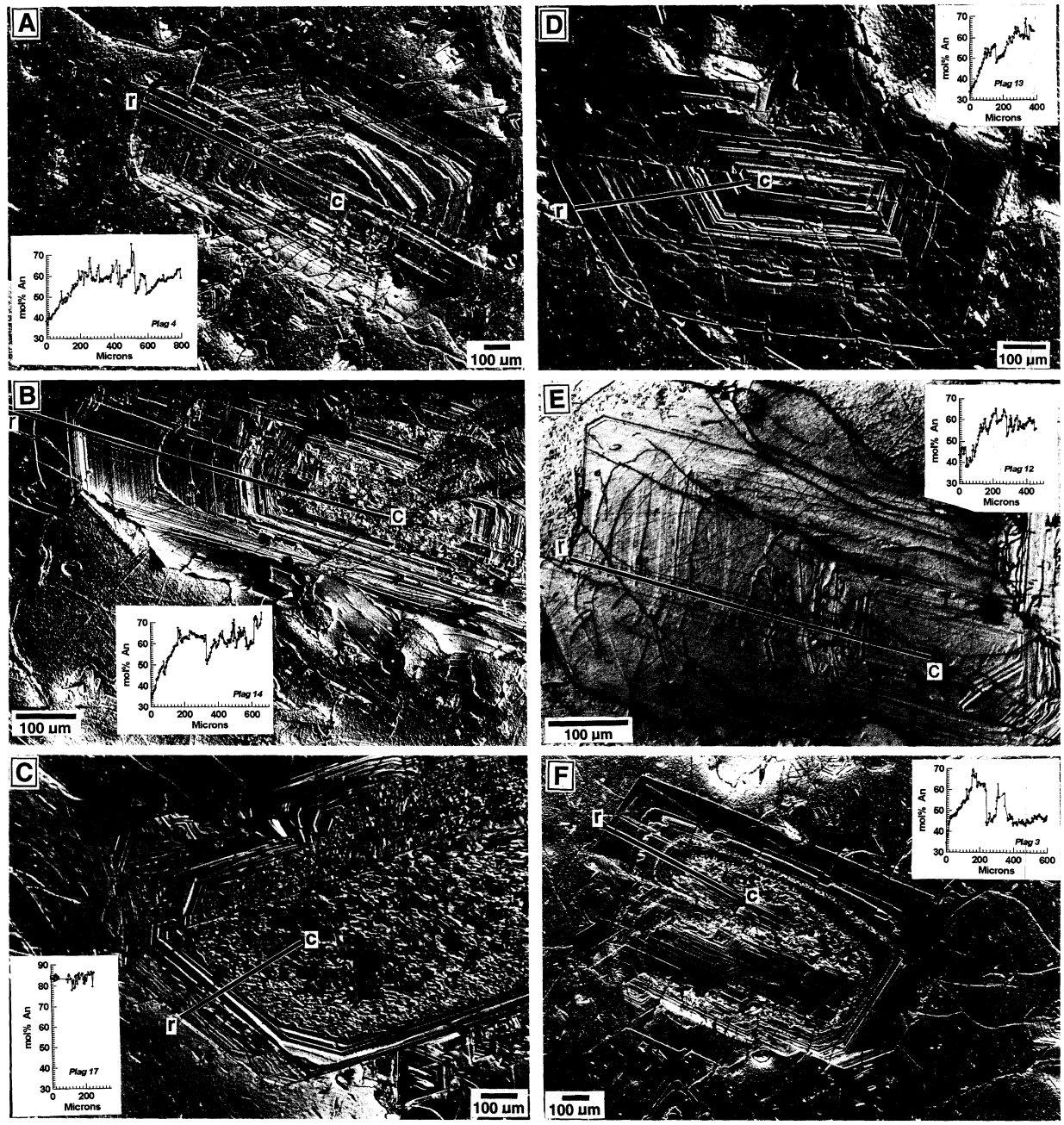


Fig. 5. NDIC images and EPMA profiles of An content vs. distance from the rim (micrometers) for six plagioclase grains in San Pedro dacite sample H-16. Note that the scale of the An profiles does not match those of the photomicrographs. Cores (c) and rims (r) of the EPMA traverses are marked on the images. The phenocrysts (**A**, **B**, **D**, **E**, and **F**) have oscillatory zoned intervals separated by pronounced unconformities at one or more major dissolution surfaces. Steep gradients in An content commonly occur coreward of abrupt shifts in An corresponding to the dissolution surfaces. The calcic xenocryst (**C**) has a sieve-textured core overgrown by an oscillatory zoned mantle and rim.

content but by high FeO′ contents, 0.58 ± 0.17 wt% (Fig. 4).

### Representative crystals?

Subvolcanic magma chambers develop gradients in temperature, crystallinity, volatile content, and composition that may lead to convection and redistribution of phenocrysts (e.g., Marsh, 1988). Phenocrysts that nucleate or grow in adjacent volumes of magma within thermal and chemical gradients would have different magmatic histories, yet they may be entrained by convective flow and brought into close proximity. In this sense, there

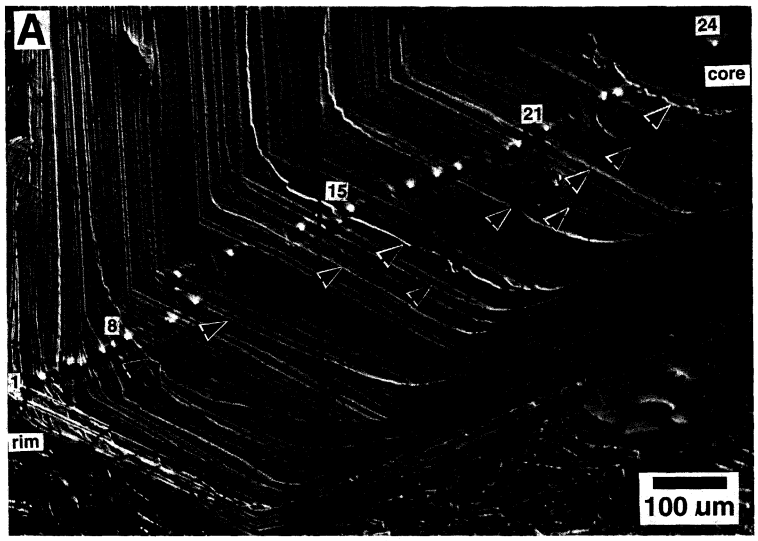
A
24
core
21
15
8
1
rim
100 µm

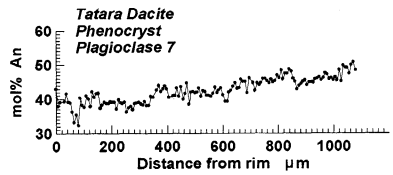
Tatara Dacite
Phenocryst
Plagioclase 7
mol% An
60
50
40
30
0
200
400
600
800
1000
Distance from rim µm

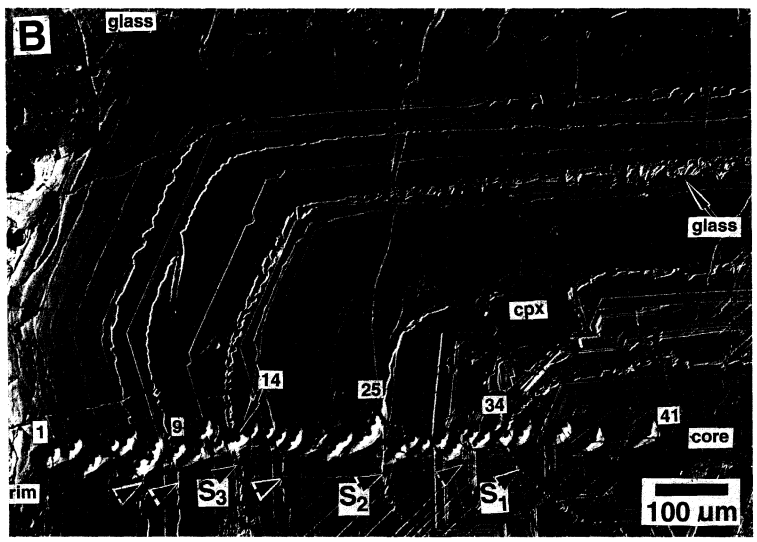
B
glass
glass
cpx
14
25
34
41
core
1
rim
S3
S2
S1
100 µm

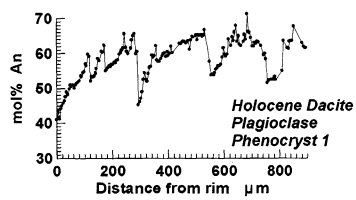
mol% An
70
60
50
40
30
0
200
400
600
800
Holocene Dacite
Plagioclase
Phenocryst 1
Distance from rim µm

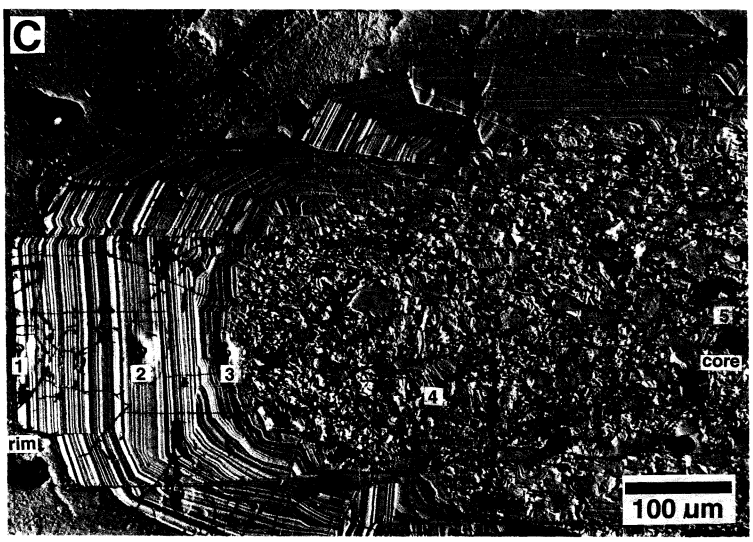
C
5
core
1
2
3
4
rim
100 µm

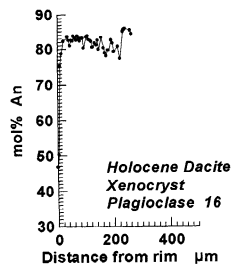
mol% An
90
80
70
60
50
40
30
0
200
400
Holocene Dacite
Xenocryst
Plagioclase 16
Distance from rim µm

are no perfectly representative phenocrysts; as magma chambers are not static and homogeneous, no two phenocrysts are exactly alike. However, cooling, compositional evolution, and convection in a chamber can impart a common set of growth and dissolution features to crystals circulating in that chamber. Typical phenocrysts have textural and compositional features characteristic of the magma chamber's history.

For example, the vast majority of phenocrysts in the Tatara dacite are remarkably similar in texture. The growth history is defined by many fine oscillatory zones punctuated by multiple subtle dissolution events. Truncations of underlying zones are conspicuous at formerly faceted corners (Fig. 6A). These common textural traits are matched by similar major element compositional profiles and compositional ranges (Figs. 3 and 4). These observations are consistent with crystallization and magmatic evolution in response to monotonic cooling of a convecting, but nonturbulent, magma body. In contrast, adjacent phenocrysts in the San Pedro dacite can be quite different from one another. Most, however, contain one or more abrupt shifts of 15 mol% An corresponding to a major dissolution surface plus several intervals of steep compositional gradient (Fig. 5). A relatively uniform population of calcic Fe-rich xenocrysts also distinguishes the San Pedro dacite (Figs. 4 and 5C). These features suggest crystallization under variable conditions quite different from those that characterized the earlier Tatara dacite magma chamber.

## SIMS ANALYSES

To explore differences in crystallization histories and magma dynamics implied by the contrasting plagioclase zoning patterns in these two lavas, SIMS analyses were obtained from a typical phenocryst in each dacite and from a xenocryst in the San Pedro dacite along traverses adjacent to EPMA traverses (Fig. 6; Table 2), with emphasis on characterizing opposite sides of dissolution surfaces.

Plagioclase no. 7 from the Tatara dacite is zoned from $An_{46}$ in the core to $An_{32}$ near the rim but has a reversely zoned rim (Fig. 6A). This crystal contains >100 euhedral oscillatory zones 1–20 $\mu$m wide, interrupted by ten dissolution surfaces, which are overgrown by slightly more An-rich plagioclase. The outermost 100–150 $\mu$m is composed of nonplanar, wavy or convolute, cross-stratified oscillatory zones (Fig. 6A). The An profile decreases gradually from $An_{45}$ to $An_{38}$ before the reverse zoned interval at the rim (Fig. 7). In the interval between the core and 180 $\mu$m from the rim, SIMS profiles, except for a few outliers, show gradual decreases in Mg, Fe, and Ti and increases in K, Sr, and Ba. The outermost 180 $\mu$m is complicated by a large oscillation in Sr, Ba, and K and increases in Fe and Ti (Fig. 7). The observed shifts in Sr and Ba across subtle resorption surfaces are small, but substantial drops correspond to the major resorption surface nearest the rim.

San Pedro phenocryst no. 1 ranges in composition from $An_{65}$ to $An_{32}$. Growth zoning characterized by ~100 planar euhedral oscillatory zones 1–20 $\mu$m wide is punctuated by four minor and three major dissolution surfaces. The major dissolution surfaces truncate a dozen or more underlying growth zones and are overgrown by plagioclase ~15 mol% more An rich than the underlying zones (Figs. 3B and 7). Trapped in ~$An_{47}$ plagioclase below the outermost major dissolution surface are elongate 10 × 30 $\mu$m inclusions of clear rhyolitic glass similar in composition to matrix glass (Table 1; Fig. 6B). Mg, Fe, and Ti contents decrease from core to rim and vary sympathetically with An content; i.e., immediately rimward of major dissolution surfaces all increase (Fig. 7). Sr, Ba, and K contents vary antithetically with An content and drop across major dissolution surfaces (Fig. 7). The outermost 50–75 $\mu$m is complicated by pronounced increases in Mg, K, and Ti and a sharp decrease in Sr (Fig. 7).

San Pedro xenocryst no. 16 is 650 $\mu$m from core to rim and contains an anhedral core with a micrometer-scale sieve texture overgrown by 50 euhedral oscillatory growth zones 1–4 $\mu$m wide (Fig. 6C). This xenocryst shows little compositional zoning, with core, mantle, and rim between $An_{76}$ and $An_{82}$. Because of the sieve texture and a lack of major element variability in this and other xenocrysts (Figs. 5C and 6C), SIMS data were acquired from five spots. With the exception of Ti, and perhaps Mg, fluctuations in trace element abundances are slight. The xenocryst has considerably higher Mg, Fe, and Ti and lower K, Ba, and Sr abundances than any part of San Pedro phenocryst no. 1 (Fig. 7).

## ORIGIN OF TEXTURAL AND CHEMICAL ZONING

### Oscillatory zoning

The fine-scale 1–20 $\mu$m wide euhedral oscillatory zones that comprise the bulk of the plagioclase phenocrysts are thought to reflect incremental diffusion-controlled growth

←

Fig. 6. NDIC images and EPMA traverses of plagioclase crystals analyzed by SIMS. The EPMA profiles were measured along the traverses marked by the ion probe pits. (**A**) Phenocryst in the Tatara dacite. In this and following images, arrows indicate dissolution surfaces where underlying euhedral oscillatory zones are truncated. The EPMA traverse shows small shifts in An content at each subtle dissolution surface. Selected ion probe analytical spots are numbered (see Table 2). Isotopic analyses were performed after the beam width was narrowed such that most sputtering was occurring from the innermost ~10 $\mu$m diameter pit in each depression. (**B**) Phenocryst in the San Pedro dacite. Arrows marked $S_1$, $S_2$, and $S_3$ denote major dissolution surfaces associated with large changes in An content and nonbinary element concentrations (Fig. 7). Small rhyolitic glass inclusions are trapped just below $S_3$. (**C**) Xenocryst in the San Pedro dacite. Euhedral oscillatory zones have overgrown the anhedral sieve-textured core. Because of the uniform major element composition, only five SIMS spots were analyzed.

**TABLE 2.** SIMS analyses of plagioclase crystals

| Spot no. | Position (μm) | wt% oxides | | | | | mol% An | ppm | | | |
|---|---|---|---|---|---|---|---|---|---|---|---|
| | | $Na_2O$ | $Al_2O_3$ | CaO | $K_2O$ | FeO* | | Sr | Ba | Ti | Mg |
| **San Pedro dacite phenocryst** | | | | | | | | | | | |
| P1-1 | 20 | 9.06 | 24.82 | 8.20 | 0.326 | 0.264 | 31.9 | 1480 | 452 | 107 | 139 |
| P1-2 | 45 | 7.76 | 26.52 | 9.68 | 0.178 | 0.261 | 39.5 | 1782 | 404 | 79 | 80 |
| P1-3 | 72 | 7.32 | 27.07 | 10.76 | 0.173 | 0.287 | 43.5 | 1844 | 366 | 96 | 125 |
| P1-4 | 100 | 6.10 | 28.17 | 11.73 | 0.136 | 0.362 | 50.2 | 1812 | 270 | 95 | 163 |
| P1-5 | 115 | 5.56 | 28.79 | 12.29 | 0.114 | 0.392 | 53.7 | 1727 | 238 | 98 | 178 |
| P1-6 | 130 | 5.34 | 28.96 | 12.68 | 0.116 | 0.409 | 55.4 | 1723 | 222 | 92 | 205 |
| P1-7 | 145 | 5.93 | 28.46 | 12.34 | 0.129 | 0.388 | 52.2 | 1739 | 246 | 96 | 204 |
| P1-8 | 150 | 5.57 | 28.73 | 12.13 | 0.116 | 0.387 | 53.3 | 1675 | 211 | 93 | 206 |
| P1-9 | 185 | 5.68 | 28.59 | 12.37 | 0.112 | 0.394 | 53.3 | 1681 | 217 | 98 | 207 |
| P1-10 | 215 | 5.44 | 28.90 | 12.24 | 0.113 | 0.392 | 54.1 | 1713 | 223 | 135 | 205 |
| P1-11 | 228 | 5.20 | 29.26 | 12.58 | 0.110 | 0.448 | 55.9 | 1669 | 196 | 93 | 229 |
| P1-12 | 245 | 4.69 | 29.82 | 13.14 | 0.094 | 0.478 | 59.5 | 1632 | 180 | 95 | 251 |
| P1-13 | 263 | 4.81 | 29.60 | 13.17 | 0.102 | 0.480 | 58.9 | 1608 | 185 | 100 | 266 |
| P1-14 | 270 | 5.19 | 29.14 | 12.82 | 0.123 | 0.426 | 56.4 | 1611 | 217 | 87 | 222 |
| P1-15 | 290 | 6.55 | 27.73 | 10.69 | 0.155 | 0.314 | 46.0 | 1603 | 286 | 84 | 176 |
| P1-16 | 310 | 6.30 | 28.20 | 11.61 | 0.138 | 0.347 | 49.1 | 1709 | 281 | 95 | 175 |
| P1-17 | 325 | 5.10 | 29.32 | 12.55 | 0.108 | 0.403 | 56.3 | 1637 | 210 | 94 | 203 |
| P1-18 | 342 | 5.09 | 29.24 | 12.55 | 0.107 | 0.404 | 56.4 | 1622 | 198 | 101 | 214 |
| P1-19 | 373 | 4.99 | 29.48 | 12.94 | 0.111 | 0.430 | 57.6 | 1575 | 193 | 96 | 222 |
| P1-20 | 378 | 5.11 | 29.52 | 13.15 | 0.115 | 0.441 | 57.4 | 1537 | 192 | 111 | 268 |
| P1-21 | 400 | 4.44 | 30.06 | 13.37 | 0.090 | 0.471 | 61.2 | 1520 | 168 | 103 | 245 |
| P1-22 | 415 | 4.49 | 30.01 | 13.42 | 0.089 | 0.476 | 61.0 | 1492 | 166 | 102 | 248 |
| P1-23 | 432 | 4.31 | 30.18 | 13.64 | 0.081 | 0.499 | 62.4 | 1464 | 164 | 103 | 258 |
| P1-24 | 450 | 4.27 | 30.33 | 13.80 | 0.078 | 0.514 | 62.9 | 1482 | 154 | 96 | 254 |
| P1-25 | 455 | 4.19 | 30.37 | 14.12 | 0.072 | 0.500 | 63.9 | 1537 | 156 | 93 | 245 |
| P1-26 | 462 | 4.32 | 30.52 | 14.18 | 0.090 | 0.500 | 63.3 | 1545 | 171 | 103 | 259 |
| P1-27 | 489 | 5.90 | 28.55 | 12.05 | 0.124 | 0.372 | 51.7 | 1681 | 243 | 92 | 207 |
| P1-28 | 508 | 5.32 | 29.10 | 12.29 | 0.096 | 0.391 | 54.9 | 1581 | 206 | 93 | 165 |
| P1-29 | 526 | 4.89 | 29.55 | 13.04 | 0.091 | 0.450 | 58.3 | 1586 | 184 | 98 | 199 |
| P1-30 | 545 | 4.48 | 30.24 | 13.65 | 0.080 | 0.479 | 61.6 | 1541 | 183 | 97 | 176 |
| P1-31 | 565 | 4.79 | 29.67 | 13.30 | 0.097 | 0.412 | 59.3 | 1572 | 198 | 97 | 167 |
| P1-32 | 577 | 4.50 | 30.03 | 13.38 | 0.080 | 0.489 | 61.0 | 1511 | 161 | 98 | 222 |
| P1-33 | 586 | 4.05 | 30.69 | 14.05 | 0.070 | 0.503 | 64.6 | 1501 | 147 | 96 | 212 |
| P1-34 | 608 | 4.60 | 29.97 | 13.26 | 0.084 | 0.476 | 60.2 | 1530 | 169 | 104 | 229 |
| P1-35 | 620 | 4.69 | 29.86 | 13.40 | 0.089 | 0.496 | 60.0 | 1537 | 166 | 166 | 269 |
| P1-36 | 629 | 4.68 | 29.76 | 13.42 | 0.110 | 0.492 | 60.0 | 1594 | 178 | 116 | 243 |
| P1-37 | 632 | 5.65 | 28.83 | 12.37 | 0.115 | 0.395 | 53.4 | 1628 | 220 | 92 | 201 |
| P1-38 | 655 | 6.02 | 28.34 | 11.48 | 0.122 | 0.334 | 50.0 | 1678 | 240 | 90 | 182 |
| P1-39 | 709 | 4.26 | 30.44 | 14.05 | 0.093 | 0.538 | 63.3 | 1571 | 150 | 109 | 284 |
| P1-40 | 755 | 4.82 | 30.07 | 13.26 | 0.098 | 0.510 | 59.1 | 1576 | 156 | 111 | 288 |
| P1-41 | 825 | 4.78 | 29.75 | 12.96 | 0.097 | 0.507 | 58.7 | 1611 | 213 | 116 | 312 |
| **San Pedro xenocryst** | | | | | | | | | | | |
| P16-1 | 10 | 2.69 | 32.41 | 16.44 | 0.056 | 0.660 | 76.2 | 1192 | 82 | 195 | 495 |
| P16-2 | 120 | 1.97 | 33.70 | 17.29 | 0.039 | 0.624 | 82.2 | 1168 | 55 | 150 | 456 |
| P16-3 | 190 | 2.12 | 33.40 | 17.33 | 0.045 | 0.652 | 81.1 | 1254 | 73 | 195 | 507 |
| P16-4 | 300 | 2.14 | 33.48 | 17.30 | 0.048 | 0.628 | 80.9 | 1264 | 69 | 160 | 443 |
| P16-5 | 635 | 2.38 | 33.10 | 16.93 | 0.067 | 0.650 | 78.8 | 1244 | 75 | 196 | 438 |
| **Tatara phenocryst** | | | | | | | | | | | |
| P7-1 | 25 | 7.23 | 27.13 | 10.09 | 0.287 | 0.385 | 41.9 | 1636 | 326 | 156 | 89 |
| P7-2 | 60 | 7.98 | 26.56 | 9.10 | 0.295 | 0.321 | 37.1 | 1621 | 394 | 137 | 98 |
| P7-3 | 110 | 9.15 | 25.37 | 7.89 | 0.327 | 0.287 | 30.9 | 1491 | 501 | 147 | 96 |
| P7-4 | 130 | 8.57 | 26.02 | 8.80 | 0.269 | 0.299 | 34.8 | 1568 | 463 | 132 | 105 |
| P7-5 | 140 | 7.97 | 26.55 | 9.27 | 0.226 | 0.298 | 37.8 | 1753 | 415 | 124 | 113 |
| P7-6 | 145 | 8.09 | 26.59 | 9.50 | 0.214 | 0.301 | 38.0 | 1789 | 427 | 120 | 116 |
| P7-7 | 158 | 8.28 | 26.34 | 9.22 | 0.213 | 0.291 | 36.8 | 1804 | 441 | 125 | 123 |
| P7-8 | 180 | 7.83 | 26.75 | 9.55 | 0.196 | 0.289 | 38.9 | 1775 | 398 | 117 | 122 |
| P7-9 | 210 | 8.33 | 26.31 | 8.99 | 0.211 | 0.289 | 36.0 | 1933 | 545 | 130 | 127 |
| P7-10 | 270 | 8.27 | 26.38 | 9.08 | 0.204 | 0.291 | 36.5 | 1939 | 527 | 124 | 128 |
| P7-11 | 300 | 8.52 | 26.16 | 8.73 | 0.212 | 0.288 | 34.9 | 1975 | 572 | 137 | 132 |
| P7-12 | 370 | 8.32 | 26.32 | 8.90 | 0.204 | 0.309 | 35.9 | 2108 | 527 | 153 | 145 |
| P7-13 | 470 | 7.89 | 26.76 | 9.49 | 0.180 | 0.316 | 38.6 | 1938 | 446 | 141 | 145 |
| P7-14 | 515 | 7.90 | 26.74 | 9.49 | 0.182 | 0.317 | 38.6 | 1916 | 442 | 139 | 145 |
| P7-15 | 540 | 8.19 | 26.41 | 9.26 | 0.192 | 0.300 | 37.2 | 1972 | 485 | 187 | 145 |
| P7-16 | 630 | 7.99 | 26.63 | 9.28 | 0.183 | 0.318 | 37.8 | 1981 | 467 | 145 | 148 |
| P7-17 | 670 | 7.70 | 26.90 | 9.63 | 0.175 | 0.320 | 39.6 | 1972 | 451 | 139 | 152 |
| P7-18 | 695 | 7.98 | 26.51 | 9.39 | 0.183 | 0.295 | 38.1 | 2045 | 492 | 141 | 140 |
| P7-19 | 770 | 7.43 | 27.16 | 9.79 | 0.176 | 0.327 | 40.8 | 1882 | 370 | 145 | 132 |
| P7-20 | 780 | 7.34 | 27.21 | 10.17 | 0.171 | 0.347 | 42.1 | 1940 | 371 | 162 | 139 |
| P7-21 | 825 | 7.45 | 26.98 | 9.86 | 0.176 | 0.340 | 40.9 | 1910 | 393 | 142 | 132 |
| P7-22 | 910 | 6.82 | 27.63 | 10.46 | 0.146 | 0.331 | 44.6 | 1951 | 354 | 161 | 151 |
| P7-23 | 930 | 6.55 | 30.17 | 10.24 | 0.138 | 0.345 | 45.0 | 1843 | 328 | 157 | 157 |
| P7-24 | 1080 | 7.10 | 27.45 | 10.25 | 0.158 | 0.363 | 43.1 | 1836 | 290 | 166 | 162 |

*Note:* position is in micrometers from the rim.

in response to near-equilibrium additions to the crystal surface via the adjacent melt boundary layer (e.g., Sibley et al., 1976; Haase et al., 1980; Pearce and Kolisnik, 1990). This type of zoning implies steady-state cooling, crystal growth at low undercooling, and negligible melt convection within the diffusion boundary layer. Nearly straight boundaries between sector zones are common in Tatara phenocrysts (Fig. 3) and further suggest a uniform growth rate over much of the lifetime of these crystals (Philpotts, 1990). The convolute zones near the rim of Tatara phenocryst no. 7 (Fig. 6A) are unusual and may reflect changes in kinetic parameters or convection of the melt during crystal growth.

### Dissolution surfaces and composition

Temperature and melt $H_2O$ content are the principal controls on plagioclase composition and stability in calc-alkaline magmas (Housh and Luhr, 1991; Rutherford and Devine, 1988). Depression of the plagioclase liquidus with increasing $H_2O$ causes the An content of plagioclase in equilibrium with a melt to increase (Housh and Luhr, 1991). In a small subvolcanic body of hydrous magma, crystal settling or chamberwide convection could transport phenocrysts through modest pressure gradients sufficient to change melt $H_2O$ content and thereby affect plagioclase dissolution. For example, Rutherford and Devine's (1988) experiments show that in a dacitic magma at 2.2 kbar, increasing the pressure 10% (220 bars) increases the An content of plagioclase 3–4 mol%. This pressure change requires downward transport of crystals through ~600 m of magma. Rapid devolatilization during an eruption or influxes of $H_2O$ from subjacent basaltic magma may also be viewed as potential agents of plagioclase dissolution or compositional change.

Smooth dissolution surfaces truncating underlying planar oscillatory zones, such as those observed in the Tatara dacite phenocrysts (Figs. 3 and 6A), are described by Pearce and Kolisnik (1990) and have been reproduced in experiments by Tsuchiyama (1985) and Sunagawa (1992). Heating of a multicomponent melt in equilibrium with plagioclase by only 5–10 °C is sufficient to produce rounding of faceted corners by diffusive dissolution of the crystal, the rate and extent of dissolution being proportional to the temperature increase. Tsuchiyama termed this "simple dissolution," and the phenomenon is remarkably illustrated in Sunagawa's in situ heating experiments. In contrast, immersion of albite-rich plagioclase in a hotter melt in equilibrium with more anorthitic plagioclase produces a reaction that penetrates the albitic plagioclase and forms an An-rich sieve-textured overgrowth on the albitic core. This is Tsuchiyama's "partial dissolution," which has long been recognized as an indicator of mixing basaltic and silicic magma (Eichelberger, 1978). Homma (1932) recognized the importance of simple dissolution features, and judging from many recent illustrations of plagioclase zoning in arc lavas (Nixon and Pearce, 1987; Pearce et al., 1987; Stamatelopoulou-Seymour et al., 1990; Singer et al., 1993), simple dissolution surfaces are more common than partial dissolution and reaction textures (e.g., Eichelberger, 1978). Dissolution surfaces identified in Tatara and San Pedro dacite phenocrysts (Figs. 3, 5, 6A, and 6B) are of the simple type and are best explained by heating of the melt phase. Although the role of $H_2O$ in the dissolution of plagioclase has not been documented experimentally, consistently more An-rich overgrowths on the dissolution surfaces could reflect temperature increases attended by subtle increases in melt $H_2O$ content. The problem concerning the Tatara dacite phenocrysts is to explain rhythmic episodes of dissolution in response to changing temperature and possibly $H_2O$ content of the host melt such that these episodes affected nearly all erupted phenocrysts in a similar way. Repeated heating of phenocrysts may be caused by convective cycling (Homma, 1932) or by multiple injections of hot magma into a chamber (Sparks and Marshall, 1986). Minimal nonbinary element compositional shifts across the dissolution surfaces in the Tatara dacite phenocryst (Fig. 7) suggest that convective cycling without magma mixing was important.

The major dissolution surfaces $S_1$, $S_2$, and $S_3$ in the San Pedro phenocryst preceded 12–15 mol% increases in An content (Fig. 6B). Although these abrupt compositional shifts could reflect episodic increases in $H_2O$ content of the host melt, it is difficult to envision that $H_2O$ alone is the agent of this zoning pattern because in the San Pedro phenocryst Mg, Fe, and Ti abundances increase and Sr and Ba abundances decrease following each dissolution event (Fig. 7). Experiments of Longhi et al. (1976) suggest that possible effects of plagioclase composition on $D_{MgO}^{plag/melt}$ are small, thus changes in An content caused by shifting $H_2O$ concentration in the melt are unlikely to change MgO concentration in the plagioclase. Although $D_{Sr}^{plag/melt}$ and $D_{Ba}^{plag/melt}$ are strongly dependent on plagioclase An content (Blundy and Wood, 1991; see Eqs. 2 and 3 below), measured Sr and Ba concentrations in the plagioclase immediately rimward of dissolution surfaces $S_1$, $S_2$, and $S_3$ are 20–30% higher than can be explained solely by the observed increases in An content (Fig. 7). Because changing An content as a consequence of increasing melt $H_2O$ content cannot alone explain the observed nonbinary element concentrations bracketing these dissolution surfaces, other factors must be involved. A substantial and abrupt change in the composition of the host melt to higher Mg, Fe, Sr, and Ti and lower K and Ba contents following each major dissolution event is consistent with the observed nonbinary element concentrations. In this light, major plagioclase dissolution events in the San Pedro magma chamber are consistent with mingling, thermal equilibration leading to plagioclase dissolution, and localized chemical mixing of hydrous basaltic magma and the silicic melt hosting the plagioclase phenocrysts.

### Glass inclusions

Small inclusions of rhyolitic glass are trapped along the outermost major dissolution surface in many San Pedro phenocrysts (e.g., Fig. 6B). Except for $Na_2O$, which is substantially lower in content in the inclusion reflecting possible Na loss during EPMA, the trapped inclusion glass is remarkably similar to that of the host matrix glass (Table 1). Apparently, the phenocryst in Figure 6B was im-

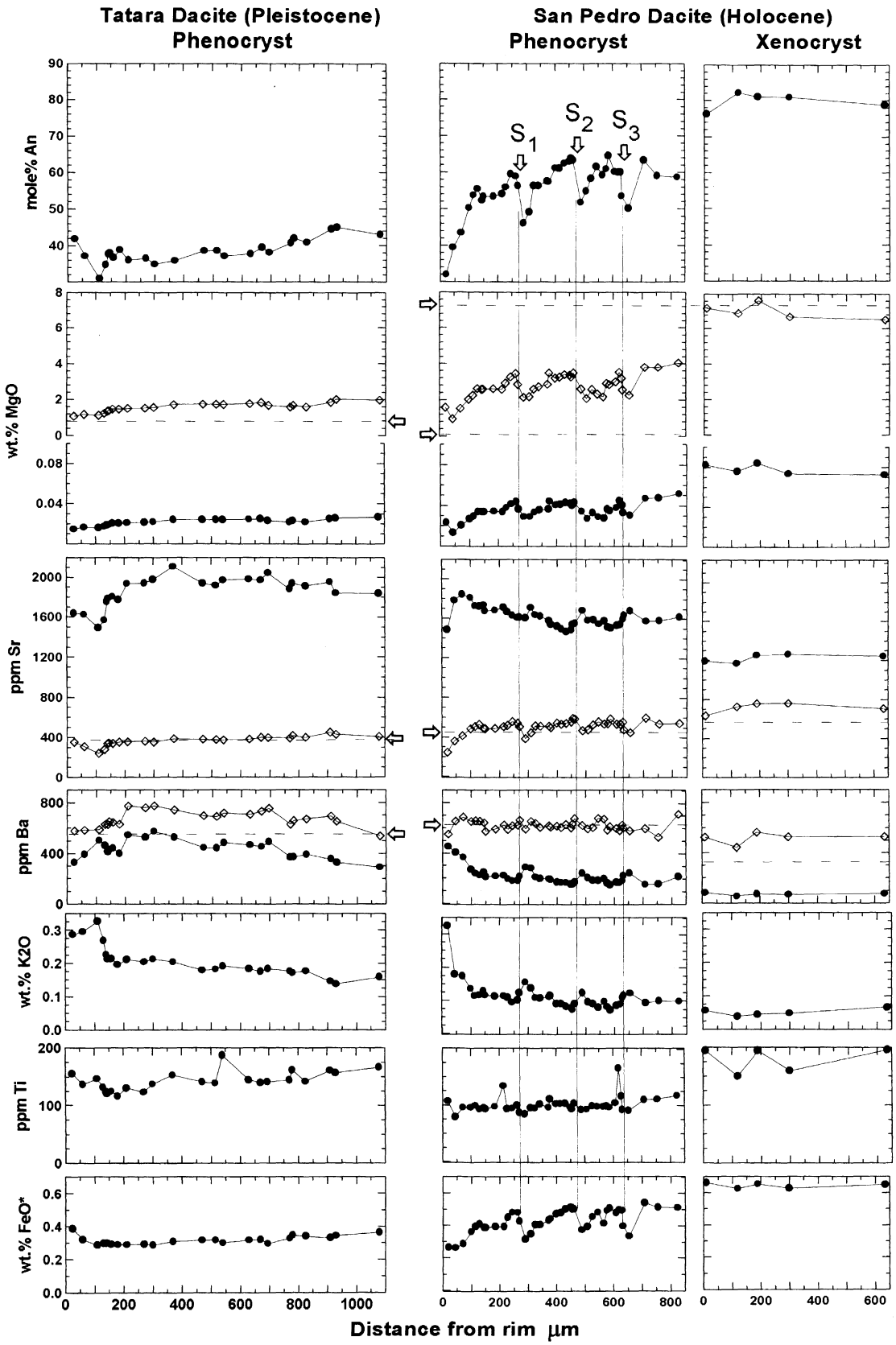
Tatara Dacite (Pleistocene)
Phenocryst
San Pedro Dacite (Holocene)
Phenocryst
Xenocryst
S1
S2
S3
mole% An
wt.% MgO
ppm Sr
ppm Ba
wt.% K2O
ppm Ti
wt.% FeO*
Distance from rim μm

mersed in a rhyolitic melt with high $SiO_2$ and $K_2O$ contents and low CaO and MgO contents prior to the last dissolution event and before growth of its outermost 220 $\mu$m. As they occur in sodic plagioclase ($\sim An_{47}$) in a zone of steep normal compositional gradient, these inclusions were probably trapped during rapid crystal growth at high undercooling (e.g., Lofgren, 1980; Anderson, 1984). The undercooling event was followed closely by heating, dissolution, and renewed growth of the crystal. As noted above, growth renewed from a melt that was probably much richer in Mg, Sr, Ti, and Fe and poorer in K and Ba than the trapped rhyolitic melt. We interpret the rhyolitic glass inclusions as the transient residual liquid composition resulting from a cycle of crystal fractionation and melt evolution that preceded the last major dissolution and magma mixing event. The MgO concentration in the inclusion and matrix glass is about 0.1 wt% (Table 1). Using the expression for $D_{Mg}^{plag/melt}$ in Equation 1, the plagioclase in equilibrium with these glasses ($T$ = 950 °C) should contain roughly 0.005 wt% MgO, which is much lower than the concentrations measured at the phenocryst rim (0.023 wt%) or adjacent to the trapped inclusions (0.029 wt%). This discrepancy can be reconciled, in part, if phenocryst rims and internal sodic zones containing melt inclusions reflect rapid growth. As discussed below, for a strongly incompatible element such as Mg, rapid crystal growth increases the effective partition coefficient, thus elevating Mg concentrations in the crystal (e.g., Sato, 1989).

### Sieve textures

The sieve-textured cores of the xenocrysts (Figs. 5C and 6C) are problematic. The anhedral form and spongy texture with micrometer-scale inclusions of glass and minerals suggest a reaction between preexisting plagioclase and melt (Tsuchiyama, 1985). As there are no major chemical changes within the sieve-textured zone or between the sieve-textured zones and the oscillatory zoned overgrowths, these particular crystals do not reflect magma mixing as has been suggested by some authors (e.g., Kawamoto, 1992). Rapid decompression through several kilobars is another mechanism that may cause resorption of plagioclase without large compositional changes (Nelson and Montana, 1992; Pearce et al., 1987). Although sieve textures developed in their experiments are much coarser than in the San Pedro xenocrysts, the presence of $H_2O$ may enhance fine-scale dissolution, and gradual degassing may dampen compositional changes (Nelson and Montana, 1992). Decompression and gradual loss of volatiles from plagioclase-saturated basalt during ascent from deep crustal levels into the shallow San Pedro magma chamber could be responsible for the anhedral sieve cores. In this scenario, oscillatory zoned mantles overgrew the resorbed cores during steady-state isobaric cooling after dense basaltic magma ponded beneath less dense dacitic magma resident in the San Pedro chamber.

### Melt evolution profiles

Crystallization of plagioclase can be a nonequilibrium process involving large kinetic effects due to variations in intensive parameters. Blundy and Wood (1991) and Blundy and Shimizu (1991) inferred equilibrium concentrations of Sr and Ba in melt from measured concentrations in plagioclase by dismissing as minor the potential for nonequilibrium effects. Albarede and Bottinga (1972) and Shimizu (1983) cautioned that diffusion rate controlled crystal-melt interface kinetics can lead to large deviations from equilibrium partitioning and therefore may strongly influence chemical zoning in crystals. Accordingly, we first describe inferred equilibrium melt profiles and then evaluate nonequilibrium processes before drawing conclusions about melt evolution from plagioclase phenocrysts.

We used the following partitioning expressions to calculate equilibrium melt compositions from measured concentrations in the plagioclase crystals (Blundy and Wood, 1991; Longhi et al., 1976; Nagasawa and Schnetzler, 1971; Schnetzler and Philpotts, 1970), where R is the gas constant, $T$ is absolute temperature in kelvin, $D'$ is the mole fraction ratio, $D$ the weight fraction ratio, and $X_{An}$ is the mole fraction of An component in the plagioclase:

$$R \ln D_{Mg}^{plag\text{-}melt} = 23.3/T - 0.04 \quad (1)$$

$$RT \ln D_{Sr}^{plag\text{-}melt} = 26.8 - 26.7X_{An} \quad (2)$$

$$RT \ln D_{Ba}^{plag\text{-}melt} = 10.2 - 38.2X_{An} \quad (3)$$

$$D_{K}^{plag\text{-}melt} = 0.09 \text{ (dacite); } 0.16 \text{ (basalt).} \quad (4)$$

The partitioning expressions reflect a weak temperature dependence for plagioclase-melt Mg partitioning (Longhi et al., 1976) and a strong dependence on An content for Ba and Sr. Blundy and Wood (1991) concluded that the differing elasticity of the albite and anorthite structures (thus plagioclase binary composition) governs Sr and Ba partitioning. Although $T$ varies as a crystal grows, $D_{Sr}$, $D_{Ba}$, and $D_{Mg}$ are insensitive to changes of less than several hundred degrees (Blundy and Wood, 1991; Longhi

←

Fig. 7. Compositional profiles for An, MgO, Sr, Ba, $K_2O$, Ti, and total Fe as FeO (indicated as FeO*) obtained by SIMS from crystals in Fig. 6. Solid circles are concentrations measured in the plagioclase. Open diamonds are calculated equilibrium melt compositions (see text). Vertical arrows and solid lines denote the position of major dissolution surfaces ($S_1$, $S_2$, and $S_3$ in Fig. 6B). Note the change in MgO scale for the crystal and melt profiles. Also shown by horizontal arrows and dashed lines are the bulk rock concentrations of MgO, Sr, and Ba for the two dacites and a quenched inclusion in the San Pedro dacite (Table 1; note that matrix glass MgO is plotted for the San Pedro dacite).

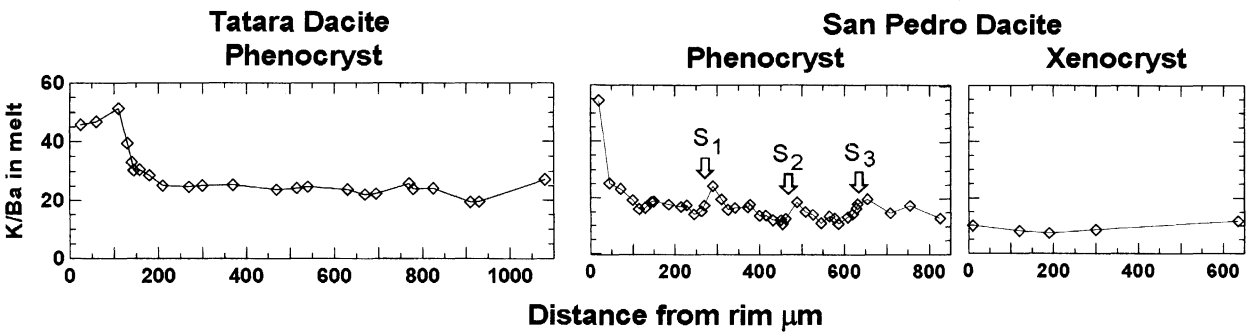


Fig. 8. Equilibrium K/Ba in melt calculated from concentrations measured in the crystals (Fig. 7). Elevated K/Ba values near the phenocryst rims record changes in the apparent partition coefficient for K owing to rapid growth. Changes in melt K/Ba recorded by oscillatory zoned intervals between major dissolution events in the San Pedro phenocryst ($S_1$, $S_2$, $S_3$; Fig. 6B) imply that open-system processes repeatedly affected melts that precipitated this crystal. In this case, mixing between low K/Ba basalt, such as that which precipitated the xenocryst, and high K/Ba dacitic or rhyolitic melt is inferred.

et al., 1976). The thermal and compositional dependencies of $D_K^{plag\text{-}melt}$ remain uncertain, but we consider that over the limited ranges considered here, Equation 4 gives a useful estimate. Using Equations 1–4 and assuming $T$ = 950 °C for the dacitic magmas and 1150 °C for the basaltic melt that precipitated the San Pedro xenocryst (Table 1), the equilibrium concentrations of Mg, Sr, Ba, and K (not shown) in the melt corresponding to the measured spots along the profiles have been calculated (Fig. 7).

The melt evolution profile calculated from the Tatara dacite phenocryst shows gradual decreases in Mg and Sr and an irregular increase in Ba from core to rim. Deviations occur near the rim (Fig. 7). The melt profile for the San Pedro dacite phenocryst is complex. Rimward of each major dissolution surface, this phenocryst apparently renewed growth from melts 50–100 ppm poorer in Ba, 0.8% poorer in $K_2O$, >100 ppm richer in Sr, and 1.5 wt% richer in MgO than the melt that precipitated the plagioclase below the surface (Fig. 7). The San Pedro xenocryst apparently grew from a basaltic melt with about 7.0% MgO, 750 ppm Sr, 0.35% $K_2O$, and 580 ppm Ba, whereas the coexisting phenocryst grew from melt that was enriched in Ba and K, and poorer in Sr and Mg, but with large ranges in composition (Fig. 7). The calculated melt concentrations agree well with bulk-lava analyses that give approximate values for the melts (Fig. 7; Table 1). The only discrepancies are the low calculated melt MgO for the San Pedro phenocryst rim relative to the matrix glass and the higher calculated melt Ba for the xenocryst relative to the bulk basaltic inclusion (Fig. 7). As noted below, the MgO discrepancy at the San Pedro phenocryst rim may reflect disequilibrium crystal growth. Using the ratios of the Ti concentrations to the average measured Ti content of each of the crystals from the bulk Tatara dacite, San Pedro dacite matrix glass, and basaltic inclusion (Table 1; Fig. 7), $D_{Ti}^{plag/melt}$ is constrained crudely at 0.03–0.04. These estimates agree well with the value determined experimentally by Phinney and Morrison (1990).

Ratios of incompatible elements such as K/Ba in bulk lavas may be used to discriminate among magmatic processes because K/Ba is insensitive to fractional crystallization (e.g., Hildreth, 1979). Variable K/Ba in comagmatic lavas suggests multiple source components or mixing of end-member melts differing in K/Ba. Ignoring for the moment the large gradients near the rims of the two phenocrysts (Fig. 8), the range in melt K/Ba calculated from the San Pedro phenocryst is twice that of the Tatara phenocryst, with large abrupt decreases following major dissolution events. This contrasts with the nearly flat melt profile from the Tatara phenocryst (Fig. 8). Assuming that equilibrium was approached, fluctuations in K/Ba imply that the San Pedro melt evolved repeatedly from low to high K/Ba prior to each major dissolution event. This could reflect crystal growth from melts created by variable degrees of diffusive chemical mixing between end-members with low (basaltic) and high (rhyolitic) K/Ba. This implies a spatial or temporal change in K/Ba of the hybrid melt as the crystal grew between dissolution events. Alternatively, disequilibrium may have been important, and rapid growth during undercooling events may have caused K to be enriched in plagioclase without affecting Ba. We show below that disequilibrium effects were probably limited to phenocryst rims and rare interior zones of the San Pedro phenocryst.

We suggest that differences in calculated melt evolution profiles for Sr, Ba, K, Mg, and K/Ba between the Tatara and San Pedro phenocrysts (Figs. 7 and 8) reflect contrasting processes and dynamics in their respective magma chambers. Kinetic effects, particularly rapid growth produced by undercooling must, however, be considered before weight is given to these interpretations.

### Role of crystallization kinetics

The equilibrium concentrations of Sr and Ba in plagioclase are a function of their abundances in the coexisting melt and the An content of the crystal (Blundy and Wood, 1991, 1992). Factors that may change the Sr and Ba concentrations in magma include closed-system equilibrium or fractional crystallization or open-system addition of new melt and magma mixing. Growing plagioclase accurately records changes in the bulk melt composition

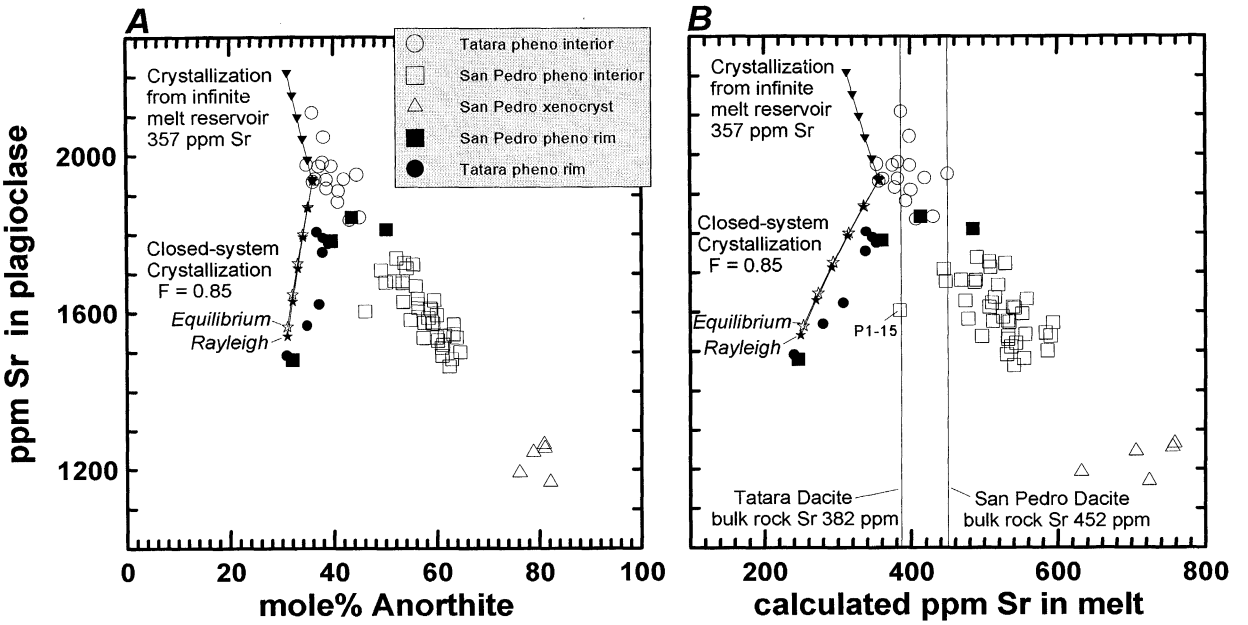


Fig. 9. Plots of Sr concentration in plagioclase measured by SIMS vs. (**A**) An content of the crystals, and (**B**) Sr concentration in the coexisting melt calculated using Eq. 2. Three crystallization models were constructed assuming $C_0^{melt}$ = 357 ppm Sr and included variable $D_{Sr}^{plag/melt}$ as An varied from $An_{36}$ to $An_{31}$. The closed-system models assumed that plagioclase composed 70 wt% of the bulk solid and that $D_{Sr}^{crystal/melt}$ for the other crystals was zero. The curves show similar effects for 15 wt% crystallization under conditions of equilibrium, with crystals remaining in contact with the host liquid (open stars), or Rayleigh fractional crystallization. Although these models reproduce evolution of the Tatara phenocryst rim, note that the calculated melts for both two phenocryst rims reach Sr concentrations 40–50% lower than the bulk rock values. One interior analysis (P1-15) from the San Pedro phenocryst is also low in Sr.

provided its rate of growth is slow enough to ensure that diffusion of trace elements through the melt maintains near-equilibrium concentrations at the melt-crystal interface. Periods of rapid crystal growth strongly deplete the diffusion boundary layer of the adjacent melt in compatible elements such as Sr and enrich the boundary layer in incompatible elements (Albarede and Bottinga, 1972). Plagioclase zones precipitated during rapid crystal growth would be depleted in Sr and enriched in K, Mg, and Ti relative to zones formed under near-equilibrium conditions. As elemental partitioning in the rapid growth case deviates from equilibrium partitioning, erroneous estimates of the bulk composition of coexisting melt could result. Substantial drops in Sr content and increases in K (plus Mg and Ti) content occur in the outermost 100–180 $\mu$m of the two dacite phenocrysts (Fig. 7) leading us to suspect that the phenocryst rims record episodes of rapid disequilibrium growth.

The difficulty lies in distinguishing effects of disequilibrium that are induced by rapid growth rate from effects of closed-system crystallization, which can also have a significant and similar effect on the evolution of trace element concentrations in the melt. Models illustrating changes in the composition of plagioclase and coexisting melt were constructed to examine the behavior of Sr in the outermost 180 $\mu$m of the Tatara dacite phenocryst (Fig. 9). Although changes in $D_{Sr}^{plag/melt}$ because of successive growth of plagioclase zones that decrease from $An_{36}$ to $An_{31}$ (Fig. 7; Table 2 analyses P7-9–P7-3) in an infinite melt reservoir cannot explain the rim compositions, simple models involving 15 wt% of closed-system equilibrium or Rayleigh crystallization appear, at first glance, to explain the Sr-An variation in the Tatara dacite phenocryst rim (Fig. 9A). However, the concentrations of Sr in calculated melts using Equation 2 for the Tatara dacite phenocryst rim decrease from 357 to 241 ppm; the final value is low compared to the bulk-rock value of 382 ppm (Fig. 9B). The rim of the San Pedro dacite phenocryst is also depleted in Sr relative to the bulk-rock value. A severe additional constraint on the application of these crystallization models is imposed by mass balance. The 100 $\mu$m wide zones recording anomalous Sr depletions represent 20–25 vol% of each of the two phenocrysts in Figure 6. These volumes translate to <2% of the total mass of the Tatara dacite and <4% of the San Pedro dacite. Thus, the equilibrium crystallization model (Fig. 9) requires a crystallized volume 3–5 times greater than can be accommodated in the phenocryst rims. We therefore interpret the low predicted Sr contents in the melt as a result of disequilibrium related to rapid growth. In this case, Equation 2 is not a valid expression of $D_{Sr}^{plag/melt}$. The Sr-poor zone within the interior in the San Pedro phenocryst (Fig. 9B; analysis P1-15, Table 2) coincides with a steep compositional gradient in which si-

licic glass inclusions were trapped (Figs. 6B and 7). Like the rims, this interval is overly depleted in Sr, and we suggest that it too reflects a period of rapid crystal growth during an earlier undercooling event within the preeruptive magma chamber. Because the equilibrium Ba partition coefficient is much closer to unity than that of Sr, Ba contents in plagioclase are less affected by rapid growth (Albarede and Bottinga, 1972); Ba is not overly enriched in the rims. However, the incompatibility of K (Eq. 4) predicts that it should be enriched in zones where Sr is depleted. Elevated K contents, manifested as remarkably high K/Ba ratios at the phenocryst rims (Fig. 8), are consistent with departures from equilibrium partitioning of K during rapid crystal growth. Abrupt increases in the highly incompatible elements Mg and Ti at the San Pedro phenocryst rim (Fig. 7) are also consistent with late rapid growth.

Quantitative treatment of kinetic effects inferred for Sr and K using diffusion boundary layer theory provides insight into the growth of the phenocryst rims. Solute-melt distribution during crystal growth is determined using the one-dimensional diffusion equation assuming a planar interface, modified to account for movement of the interface (Smith et al., 1955; Albarade and Bottinga, 1972; Shimizu, 1983):

$$d\frac{\partial^2 C_L}{\partial x^2} + V\frac{\partial C_L}{\partial x} = \frac{\partial C_L}{\partial t} \quad (5)$$

where $V$ is the crystal growth rate (interface velocity), $d$ is the diffusion coefficient of the element in the melt, $C_L$ is the concentration of the element in the melt, $x$ is the distance the interface moves into the liquid, and $t$ is time. For crystal growth into a nonconvecting infinite melt reservoir, Smith et al. (1955) solved Equation 5 for concentration in the solid as a function of distance, $C_s(x)$:

$$C_s(x) = \frac{C_0}{2}\left\{1 + \operatorname{erf}\left[\frac{\sqrt{(Vx/d)}}{2}\right] + (2D - 1)e^{-D(1-D)(Vx/d)} \cdot \operatorname{erfc}\left[\frac{(2D-1)}{2}\sqrt{(Vx/d)}\right]\right\} \quad (6)$$

where $C_0$ = initial concentration of the element in the melt adjacent to the interface at the time growth commences, and $D$ is the equilibrium crystal-melt partition coefficient. Solutions to Equation 6 illustrating the effect of rapid growth on trace element zoning may be expressed in terms of the dimensionless parameter $Vx/d$, where $x$ is the interval of rapid growth within the crystal. The strong dependence on $D$ in Equation 6 indicates that when $D$ is near 1, $C_s = C_0$ and there is no kinetic effect on partitioning, however for $D > 1$ or $D \ll 1$, the departure from equilibrium behavior is large (Shimizu, 1983). The advance of the crystal-melt interface into crystal-poor melts such as those studied here does not seriously violate the assumption of an infinite melt reservoir (Shimizu, 1983). For small increments of growth, Equation 6 gives results similar to those obtained using the numerical method required to solve Equation 5 for the finite reservoir case (Albarede and Bottinga, 1972).

The effect of growth rate on Sr concentration is illustrated by equilibrium and rapid growth models of the steep concentration gradient intervals near the rims of the Tatara and San Pedro phenocrysts (Fig. 7). Rapid growth models were calculated by choosing values for the dimensionless parameter in Equation 6 that yield the observed range of Sr concentrations (Fig. 10). Results include: (1) the effective $D_{Sr}^{plag/melt}$ can drop >30% during rapid growth of 70–100 $\mu$m of plagioclase, whereas the equilibrium $D_{Sr}^{plag/melt}$ predicted as a function of changing An content from Equation 2 may increase by >60% over this same interval, leading to a factor of two discrepancy between observed and predicted Sr concentrations (Fig. 10); (2) a mean value of $V$ in the dimensionless parameter can be calculated from these models: $V$ for the 100 $\mu$m interval of the San Pedro phenocryst and for the 70 $\mu$m interval in the Tatara phenocryst is $1 \times 10^{-9}$ cm/s; (3) using this value of $V$ and observing that the steepest gradient in K concentration in the San Pedro phenocryst occurs over a narrower, 25 $\mu$m interval ($x$), a $d^K$ value of $8 \times 10^{-9}$ cm$^2$/s is consistent with more rapid diffusion of K than Sr in silicic melts (Hofmann, 1980) and illustrates the lag effect for K enrichment relative to Sr depletion in the crystal as predicted by Shimizu (1983); (4) similar modeling for Ba shows no effect owing to rapid growth, reflecting $D_{Ba}$ values of 0.4–0.7, much closer to unity than either $D_{Sr}^{plag/melt}$ or $D_K^{plag/melt}$; and (5) abrupt increases in Mg and Ti measured in the outermost portion of the San Pedro phenocryst rim (Fig. 7) are consistent with disequilibrium caused by rapid growth because $D_{Mg}^{plag/melt}$ (0.05) and $D_{Ti}^{plag/melt}$ (0.03–0.04) are much lower than $D_K^{plag/melt}$. From Results 3 and 4, it is unlikely that the variations in K/Ba observed within the interior of the San Pedro phenocryst (Fig. 8) are caused entirely by rapid growth, as only one of these zones has anomalously low Sr.

The growth rate inferred from the phenocryst rims is remarkably similar to Cashman's (1992) estimate of 2.7 $\times 10^{-9}$ cm/s for plagioclase microlite growth in the June 1980 Mount Saint Helens dacite dome that was emplaced following the May 18, 1980, eruption. If these ~100 $\mu$m intervals of rapid phenocryst growth reflect undercooling triggered by decompression during magma ascent and eruption, the Tatara and San Pedro dacite magmas may have taken several months to ascend to the surface. This is consistent with observed eruptive timescales of dacitic magma at Mount Saint Helens (Cashman, 1988). Although all amphiboles in the Tatara dacite have opacite rims of variable thickness (Fig. 2A), the San Pedro dacite contains abundant euhedral unrimmed hornblende (Fig. 2B) and is thus at odds with Rutherford and Hill's (1993) experiments showing that, upon decompression, opacite rims develop on hornblende in a matter of days. Most Tatara phenocrysts have reversely zoned rims (Fig. 3). In the phenocryst modeled here, the outermost 80 $\mu$m also shows increasing Sr and decreasing K. This is inconsis-

tent with rapid crystal growth and may reflect growth of the outermost 80 μm during shallow storage in the conduit prior to eruption where extensive groundmass crystallization (Fig. 2A) may have complicated late-stage melt evolution. In addition, several of the outermost zones of the Tatara phenocryst have complex morphologies, suggesting possible nonequilibrium growth (Fig. 6A). In contrast, the San Pedro phenocryst probably reflects rapid crystal growth during magma ascent and quenching of the melt to glass sufficiently rapidly upon eruption (through an enlarged conduit created by collapse of the edifice) to exclude such processes. The low Sr analysis from a zone with glass inclusions in the San Pedro phenocryst (Fig. 9B) is consistent with entrapment during rapid growth. As this zone is truncated by a major dissolution surface inferred to reflect a temperature increase, rapid cooling and heating cycles prior to eruption are implied.

## Magma chamber dynamics

Considerable debate surrounds the relationships among crystallization, convection, and heat transfer within magma bodies. For example, Sparks et al. (1984), Sparks (1990), and Huppert and Turner (1991) claim that in all magma chambers, including those containing highly viscous rhyolitic melt, the appropriate Rayleigh number (Ra) reflects the initial conditions of magma emplacement integrated over the entire magma thickness and remains sufficiently large to ensure turbulent convection. The alternative view (Brandeis and Jaupart, 1986; Marsh, 1988, 1989a, 1989b) is that weak convection characterized by regular laminar flow may be driven by cooling, crystallization, and growth of a boundary layer mush zone at a magma chamber roof. The textural and nonbinary element zoning of plagioclase phenocrysts record evolving melt composition and temperature along convective flow paths and can provide insight into the convective motions within portions of the two different magma bodies. In addition to the internal features of the phenocrysts, understanding crystal-liquid motions requires estimates of plagioclase density and the viscosity and density of the melt phase, which in turn require estimates of the $H_2O$ content and temperature of the melt. Estimates of these parameters (Table 1) were calculated (details in Appendix 1) following Singer et al. (1993).

### Thermally and chemically closed Tatara chamber

We suggest that the rhythmic dissolution events observed in nearly all Tatara dacite phenocrysts (Figs. 3 and 6) and the monotonic chemical trends of plagioclase and the melt (Figs. 7 and 11) are inconsistent with turbulent convection at high Ra in a low-viscosity magma and associated phenomena such as entrainment of phenocrysts in plumes, episodic crystal settling and fractionation events, periodic overturn of a density stratified chamber, or rapid mixing of chemical heterogeneities within the chamber (Sparks et al., 1984, 1993; Martin and Nokes, 1989; Koyaguchi et al., 1990). We propose instead that these patterns reflect growth of plagioclase in convection

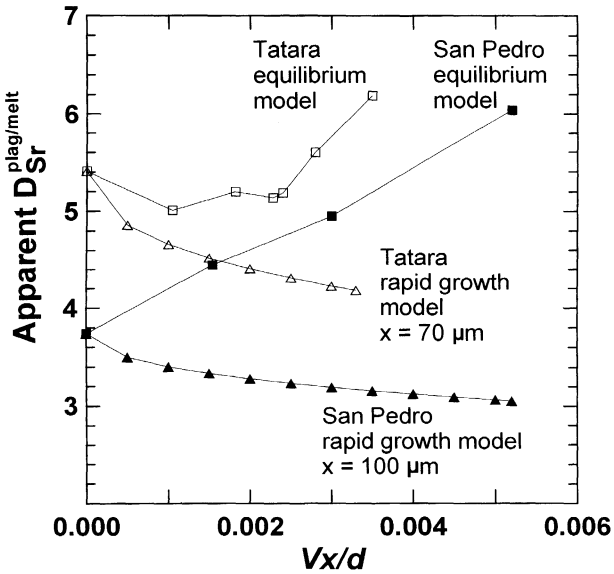


Fig. 10. Apparent $D_{Sr}^{plag/melt}$ vs. the dimensionless parameter $Vx/d$. The rapid growth models were calculated from Eq. 6 and reproduce the decreasing Sr concentrations measured at the phenocryst rims (Fig. 9). The equilibrium models were calculated from Eq. 2. The following values and assumptions have been used: $d^{Sr} = 2 \times 10^{-9}$ cm²/s (Baker, 1989); $x = 100$ μm for the San Pedro phenocryst and 70 μm for the Tatara phenocryst (intervals of steepest concentration gradients in Fig. 7); $C_0 = 485$ ppm and $D_{Sr} = 3.74$ in the San Pedro phenocryst and 357 ppm and 5.41 in the Tatara phenocryst (these were chosen by assuming that Eq. 2 provides a valid estimate of $D_{Sr}^{plag/melt}$ and melt concentration at the point where rapid crystallization begins); Sr and An concentrations from spots 100 (San Pedro) and 158 μm (Tatara) from the rims (Table 1), immediately inward from the portions of the crystals affected by rapid growth, were used in the calculations.

cells characterized by slow steady-state flow of viscous dacitic magma ($\mu \approx 10^6$ poise; Table 1) in response to a small thermal gradient. Plagioclase crystals retained during multiple cycles of convective flow (Marsh and Maxey, 1985; Marsh, 1988) underwent dissolution as they descended into the hotter interior of the magma body, whereas in the ascending cooling limbs, slow near-equilibrium plagioclase growth was renewed (e.g., Homma, 1932).

To illustrate how plagioclase phenocrysts in the Tatara dacite may be consistent with a specific pattern of steady-state laminar flow, we have constructed a rough model. The appropriate formulation of Ra depends on the thickness and temperature gradient across the inward growing thermal boundary layer (Brandeis and Jaupart, 1986; Marsh, 1989a) and is given by

$$\mathrm{Ra} = \frac{g\alpha\Delta T z^3}{\kappa\nu} \quad (7)$$

where g is gravitational acceleration, $\alpha$ is the coefficient of thermal expansion ($5 \times 10^{-5}$ °C$^{-1}$), $\Delta T$ is the temper-

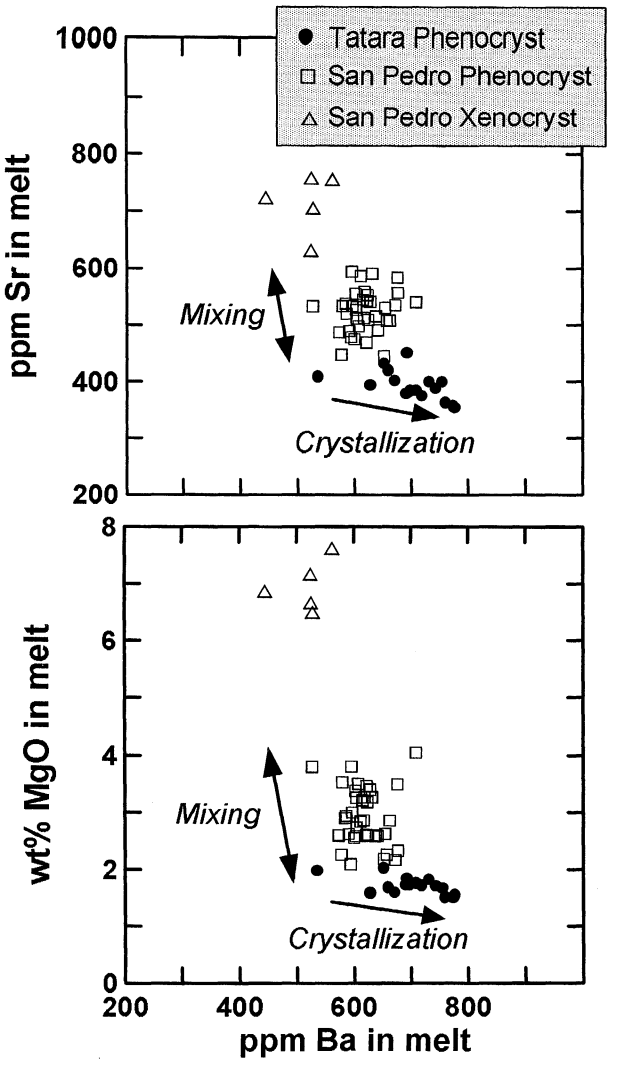


Fig. 11. Variation of Sr, MgO, and Ba in melts calculated from measured concentrations in plagioclase using Eqs. 1–3. Analyses from portions of the phenocrysts that reflect disequilibrium associated with rapid crystal growth (Fig. 9) have been removed. The large ranges in melt MgO and Sr recorded in the San Pedro phenocryst plot on possible mixing lines between basaltic melts that precipitated the xenocryst and silicic melts. In contrast, the small decreases in MgO and Sr with increasing Ba in the Tatara melts reflect crystallization of plagioclase + orthopyroxene + magnetite with buffering of Sr due to plagioclase dissolution.

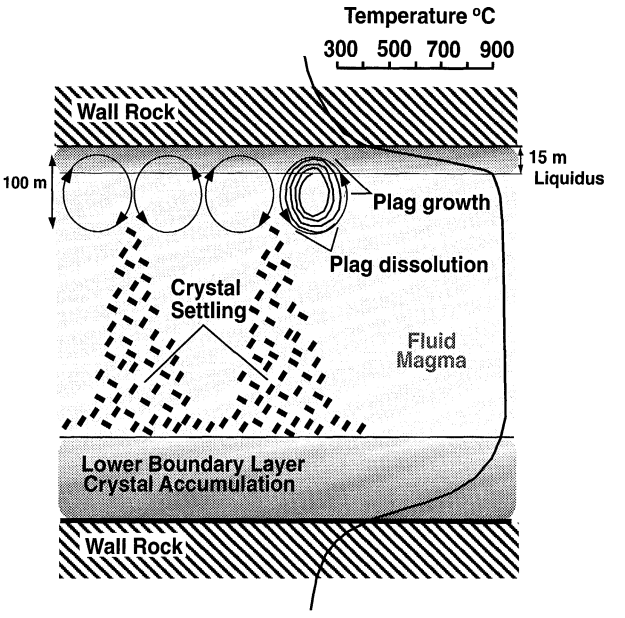


Fig. 12. Idealized model of the chemically and thermally closed Tatara magma chamber (after Brandeis and Jaupart, 1986; Marsh, 1989b). The thermal and length scales reflect calculations in the text. Circulation of plagioclase phenocrysts for hundreds of years in convective cells near the roof of a cooling sheet-like chamber at shallow crustal levels explains the periodic growth and dissolution features in Tatara dacite crystals (as in Fig. 6A) in the absence of abrupt shifts or gradients in melt composition. Increasing Ba and decreasing MgO over time in the upper part of the magma reservoir (Figs. 7 and 11) reflects the eventual gravitative settling of most plagioclase + orthopyroxene + magnetite crystals, however Sr in the upper part of the reservoir was buffered by repeated plagioclase dissolution. Eruption of the upper portion of this magma chamber could yield a phenocryst-poor lava with simply zoned plagioclase such as those in the Tatara dacite.

ature difference between the hot near-liquidus interior of the magma body and the wallrock forming the roof of the chamber, $z$ is the thickness of this boundary layer (Fig. 12), $\kappa$ is the magma thermal diffusivity ($7 \times 10^{-7}$ m$^2$/s), and $\nu$ is the kinematic viscosity ($\nu = \mu_c/\rho$). The velocity of convection in such a system is

$$U \simeq \frac{\kappa}{z}\mathrm{Ra}^b \qquad (8)$$

(Marsh, 1988), where $b$ is between ⅓ and ⅙. In the case of laminar flow, Ra must be between 200 and 300 (Marsh, 1988). As $\Delta T$ is sensitive to $z$, the depth of the chamber roof and the corresponding thermal contrast between wallrock and $T_{\text{liquidus}}$ is probably the most important parameter governing the nature of convection in an insulated chamber. For example, setting Ra = 250 in Equation 6 and assuming $\rho = 2.23$ g/cm$^3$ and $\mu_c = 10^{6.0}$ poise (Table 1; Appendix 1), if $z = 15$ m, then $\Delta T = 520$ °C, and if $z = 17$ m, $\Delta T = 357$ °C. For a $T_{\text{liquidus}} = 900$ °C (Table 1), if we choose $z = 15$ m, the wallrock temperature is about 380 °C, consistent with emplacement of the Tatara dacite in shallow crust preheated by voluminous Quaternary magmatism (Singer et al., 1994). Substituting Ra = 250 into Equation 8 with $b = ⅓$, $U$ is $10^{-6.5}$ m/s.

Assuming constant crystal growth at $10^{-11}$ cm/s (Cashman, 1990; ignoring apparently brief intervals of dissolution), $10^{10}$ s (~350 yr) were required to grow the typical Tatara phenocryst with $r = 1$ mm. If suspended in a spherical convection cell with $U = 10^{-6.5}$ m/s for $10^{10}$ s, it would have traveled ~3200 m. If each of the ten resorption surfaces in the studied phenocryst (Fig. 6A) cor-

responds to dissolution during transport through the hottest part of a convection cell, the circumference of this cell was 320 m, and its diameter was 100 m (Fig. 12). No two crystals traversed identical paths, and not all convection cells had exactly the same geometry or thermal gradient. However, most crystals retained in these cells would develop similar textural and chemical zoning. Retention of crystals in convection cells is limited and most crystals eventually settle to the floor of the chamber (Weinstein et al., 1988; Martin and Nokes, 1989; Sparks et al., 1993). Thus, <20 wt% fractional crystallization by settling of plagioclase + pyroxene + magnetite combined with plagioclase retention and dissolution (Fig. 12) can explain the gradual decrease in Mg, increase in Ba, and uniform Sr contents of melt in the uppermost portion of this magma chamber in the period preceding its eruption (Figs. 7 and 11). Evacuation of the upper 50% of a 2 km$^2$ sheet-like magma body 500 m deep, with cellular convection limited to the uppermost ~100 m, could have produced the 1 km$^3$ Tatara dacite flow.

### Thermally and chemically open San Pedro chamber

In contrast to the Tatara dacite, which was closed to inputs of new magma and heat, basaltic inclusions plus plagioclase and olivine xenocrysts indicate that a high-$T$ basaltic magma mingled with the San Pedro dacitic magma. The melt compositions calculated from the San Pedro phenocryst have ranges in Sr, Ba, Mg, and K/Ba consistent with mixing between basaltic (750 ppm Sr, 7 wt% MgO, K/Ba = 6–12) and dacitic (450 ppm Sr, 2 wt% MgO, K/Ba ≥ 20) end-members (Fig. 11). SIMS profiles (Fig. 7) show that compositional excursions characteristic of mixing occurred repeatedly during crystal growth. Because these excursions are not associated with phenocryst rims, turbulent mixing in the conduit during eruption (Koyaguchi, 1985) is ruled out as the mechanism of hybridization. Assuming plagioclase growth rates of $10^{-11}$ cm/s (Cashman, 1990), hundreds of years may have separated these mixing events from one another and from the time of eruption; i.e., injection of basalt into the San Pedro dacite did not immediately trigger explosive eruption of the dacite as has been proposed for several historic events (Pallister et al., 1992; Gourgaud et al., 1989).

The nonbinary element profiles and textures in the plagioclase phenocryst can provide details of the mixing process. Mineral equilibria and quench textures in the basaltic inclusions indicate a temperature difference of ≥200 °C between the basaltic and dacitic magmas prior to mingling (Singer and Dungan, 1992). The creation of hybrid melts by chemical mixing requires diffusive exchange of components between the end-members (e.g., Oldenberg et al., 1989). Because thermal diffusivity in a silicate melt is several orders of magnitude greater than chemical diffusivity, it is not surprising that upon basalt-dacite mingling, the initial response of plagioclase phenocrysts in the cooler dacite was simple thermal dissolution followed by renewed growth from hybrid melts. A solution of Fick's law for a diffusion couple between melt in a basaltic inclusion and its silicic host melt (Hofmann, 1980) is $C_m = C_s + \frac{1}{2}C_0 \operatorname{erfc}[x/2\sqrt{(dt)}]$, where $C_m$ is the concentration in the mixed melt, $C_s$ is the initial concentration in the silicic host to the inclusion, $C_0$ is the concentration in the basaltic melt, and $x$ is the distance from the basalt-silicic melt contact. From the calculated melt profiles (Fig. 7), $C_0$ for Sr is about 750 ppm, $C_s$ is about 450 ppm prior to each mixing event, and $C_m$ is about 600 ppm Sr in hybrid melt immediately outward from the major resorption surfaces in the phenocryst. Using these values and $d^{Sr} = 2 \times 10^{-9}$ cm$^2$/s (Baker, 1989), we find that $10^3$ yr are required to produce the 600 ppm Sr hybrid at a distance 5 cm from the basalt and $10^5$ yr are required to extend this hybrid layer 50 cm from the basalt-silicic melt contact.

Steep An gradients, trapped glass inclusions, anomalously low Sr, plus high K and K/Ba below at least one major dissolution surface in the phenocryst (Figs. 7 and 9) are consistent with periods of undercooling preceding heating and mixing events. Differences among phenocrysts (Fig. 5) that grew in the dacitic magma probably reflect the number and duration of close encounters with hot basaltic inclusions as they were mechanically comminuted and stirred into the dacite (Thompson and Dungan, 1985; Oldenberg et al., 1989). We infer that rapid heating and cooling cycles, pronounced chemical gradients, and the dispersion of phenocrysts with vastly different histories throughout the dacite reflect turbulent and chaotic convection in the sense of Sparks et al. (1984). The low settling velocities of phenocrysts in the viscous rhyolitic melt (Table 1) ensured that many phenocrysts were retained in the flow long enough to experience multiple local environments where heating and mixing took place. Although diffusional exchange on a centimeter scale between basaltic and rhyolitic melts locally produced small quantities of hybrid melt (Fig. 11), insufficient basalt was injected into the dacite to sustain mixing and generate a homogeneous andesitic hybrid (Bacon, 1986; Sparks and Marshall, 1986).

## Conclusions

The combined NDIC-EPMA-SIMS approach can resolve small but important variations in nonbinary element (Sr, Ba, Mg, Fe, Ti, and K) concentrations in plagioclase and provide the textural resolution necessary to explore the mechanisms and temporal evolution of the responsible magmatic processes. Potential applications include distinguishing thermally and chemically closed magmatic systems from open systems, constraining patterns of magmatic heat loss and convection, and quantifying the rates at which magma mixing, assimilation, and magma ascent occur. Plagioclase phenocrysts record melt compositions and kinetic effects entirely consistent with independent observations. Despite similar bulk compositions, the two dacitic lavas contain plagioclase crystals for which textures and zoning profiles indicate that the dynamic behavior of magmas feeding silicic eruptions at Volcán Tatara–San Pedro changed considerably in the intervening ~60000 yr. Contrary to previous studies, we have shown that crystallization kinetics associated with

intervals of rapid growth at relatively large undercooling can play an important role in Sr and K (plus Mg and Ti) partitioning in plagioclase. A disequilibrium growth model provides a way to estimate crystal growth rate and thus the duration of magma cooling and ascent. Kinetic effects must be identified before plagioclase zoning profiles are used to interpret the chemical and thermal evolution of a magma. More work is needed to quantify compositional and thermal dependencies of trace and minor element partitioning between plagioclase and melt (e.g., Blundy and Wood, 1994), as this would increase the confidence with which kinetic effects can be separated from compositional effects.

## Acknowledgments

This work was supported by U.S. NSF grants EAR-9019441 and EAR-9206771, plus Swiss Fonds National grant 21-36509.92 to M.A.D. and B.S.S. The UNM/SNL Ion Microprobe Facility is a joint operation of the Institute of Meteoritics of the University of New Mexico and Sandia National Laboratories that is supported in part by U.S. NSF grant EAR-9303864. We thank Dwight Deuring for assistance during the electron probe work and sample preparation. Andrew Wulff and Mike Rhodes supplied the XRF analyses. We thank an anonymous reviewer and especially J. Blundy. Each provided critical comments and useful information that helped us to improve the clarity of this paper.

## References cited

Albarede, F., and Bottinga, Y. (1972) Kinetic disequilibrium in trace element partitioning between phenocrysts and host lava. Geochimica et Cosmochimica Acta, 36, 141–156.

Anderson, A.T., Jr. (1983) Oscillatory zoning of plagioclase: Nomarski interference contrast microscopy of etched polished sections. American Mineralogist, 68, 125–129.

——— (1984) Probable relations between plagioclase zoning and magma dynamics, Fuego Volcano, Guatemala. American Mineralogist, 69, 660–676.

Bacon, C.R. (1986) Magmatic inclusions in silicic and intermediate volcanic rocks. Journal of Geophysical Research, 91, 6091–6112.

Bacon, C.R., Adami, L.H., and Lanphere, M.A. (1989) Direct evidence for the origin of low $^{18}O$ silicic magmas: Quenched samples of a magma chamber's partially-fused granitoid walls, Crater Lake, Oregon. Earth and Planetary Science Letters, 96, 199–208.

Baker, D.R. (1989) Tracer versus trace element diffusion: Diffusional decoupling of Sr concentration from Sr isotope composition. Geochimica et Cosmochimica Acta 53, 3015–3023.

Blundy, J.D., and Shimizu, N. (1991) Trace element evidence for plagioclase recycling in calc-alkaline magmas. Earth and Planetary Science Letters, 102, 178–197.

Blundy, J.D., and Wood, B.J. (1991) Crystal-chemical controls on the partitioning of Sr and Ba between plagioclase feldspar, silicate melts, and hydrothermal solutions. Geochimica et Cosmochimica Acta, 55, 193–209.

——— (1992) Reply to comment by S.A. Morse on: Partitioning of strontium between plagioclase and melt. Geochimica et Cosmochimica Acta, 56, 1739–1741.

——— (1994) Prediction of crystal-melt partition coefficients from elastic moduli. Nature, 372, 452–454.

Brandeis, G., and Jaupart, C. (1986) On the interaction between convection and crystallization in cooling magma chambers. Earth and Planetary Science Letters, 77, 345–361.

Burnham, C.W. (1979) The importance of volatile constituents. In H.S. Yoder, Ed., The evolution of the igneous rocks, fiftieth anniversary perspectives, p. 439–482. Princeton University Press, Princeton, New Jersey.

Burnham, C.W., and Davis, N.F. (1971) The role of $H_2O$ in silicate melts: I. *P-V-T* relations in the system $NaAlSi_3O_8$-$H_2O$ to 10 kilobars and 1000° C. American Journal of Science, 270, 54–79.

Cashman, K.V. (1988) Crystallization of Mount St. Helens dacite 1980–1986: A quantitative textural approach. Bulletin of Volcanology, 50, 194–209.

——— (1990) Textural constraints on the kinetics of crystallization of igneous rocks. In Mineralogical Society of America Reviews in Mineralogy, 24, 259–314.

——— (1992) Groundmass crystallization of Mount St. Helens dacite, 1980–1986: A tool for interpreting shallow magmatic processes. Contributions to Mineralogy and Petrology, 109, 431–449.

Druitt, T.H., and Bacon, C.R. (1989) Petrology of the zoned calcalkaline magma chamber of Mount Mazama, Crater Lake, Oregon. Contributions to Mineralogy and Petrology, 101, 245–259.

Eichelberger, J.C. (1978) Andesitic volcanism and crustal evolution. Nature, 275, 21–27.

Ferguson, K.M., Dungan, M.A., Davidson, J.P., and Colucci, M.T. (1992) The Tatara-San Pedro Volcano, 36°S, Chile: A chemically variable, dominantly mafic magmatic system. Journal of Petrology, 33, 1–43.

Gourgaud, A., Fichaut, M., and Joron, J.-L. (1989) Magmatology of Mt. Pelée (Martinique, F.W.I.): I. Magma mixing and triggering of the 1902 and 1929 Pelean nuées ardentes. Journal of Volcanology and Geothermal Research, 381, 43–169.

Grove, T.H., Baker, M.B., and Kinzler, R.J. (1984) Coupled CaAl-NaSi diffusion in plagioclase feldspar: Experiments and applications to cooling rate speedometry. Geochimica et Cosmochimica Acta, 48, 2113–2121.

Haase, C.S., Chadam, J., Feinn, D., and Ortoleva, P. (1980) Oscillatory zoning in plagioclase feldspar. Science, 209, 272–274.

Hildreth, W. (1979) The Bishop Tuff: Evidence for the origin of compositional zonation in silicic magma chambers. Geological Society of America Special Paper, 180, 43–75.

Hofmann, A.W. (1980) Diffusion in natural silicate melts: A critical review. In R.B. Hargraves, Ed., Physics of magmatic processes, p. 385–417. Princeton University Press, Princeton, New Jersey.

Homma, V.F. (1932) Über das ergebnis von messungen an zonaren plagioklasen aus andesiten mit hilfe des universaldrehtisches. Schweizerische Mineralogische und Petrographische Mitteilungen, 12, 345–352.

Housh, T.B., and Luhr, J.F. (1991) Plagioclase-melt equilibria in hydrous systems. American Mineralogist, 76, 477–492.

Huppert, H.E., and Sparks, R.S.J. (1988) Melting of the roof of a magma chamber containing a hot, turbulently convecting fluid. Journal of Fluid Mechanics, 188, 107–131.

Huppert, H.E., and Turner, J.S. (1991) Comments on: On convective style and vigor in sheet-like magma chambers, by B.D. Marsh. Journal of Petrology, 32, 851–854.

Kawamoto, T. (1992) Dusty and honeycomb plagioclase: Indicators of processes in the Uchino stratified magma chamber, Izu peninsula, Japan. Journal of Volcanology and Geothermal Research, 49, 191–208.

Kilinc, A., Carmichael, I.S.E., Rivers, M.L., and Sack, R.O. (1983) The ferric-ferrous ratio of natural silicate liquids equilibrated in air. Contributions to Mineralogy and Petrology, 83, 136–140.

Koyaguchi, T. (1985) Magma mixing in a conduit. Journal of Volcanology and Geothermal Research, 25, 365–369.

Koyaguchi, T., Hallworth, M.A., Huppert, H.E., and Sparks, R.S.J. (1990) Sedimentation of particles from a convecting fluid. Nature, 342, 447–450.

Lange, R.L., and Carmichael, I.S.E. (1987) Densities of $Na_2O$-$K_2O$-CaO-MgO-FeO-$Fe_2O_3$-$Al_2O_3$-$TiO_2$-$SiO_2$ liquids: New measurements and derived partial molar quantities. Geochimica et Cosmochimica Acta, 51, 2931–2946.

Lofgren, G.E. (1980) Experimental studies on the dynamic crystallization of silicate melts. In R.B. Hargraves, Ed., Physics of magmatic processes, p. 487–551. Princeton University Press, Princeton, New Jersey.

Longhi, J., Walker, D., and Hays, J.F. (1976) Fe and Mg in plagioclase. Proceedings of the Lunar Science Conference, 7, 1281–1300.

Marsh, B.D. (1981) On the crystallinity, probability of occurrence, and rheology of lava and magma. Contributions to Mineralogy and Petrology, 78, 85–98.

——— (1988) Crystal capture, sorting, and retention in convecting magma. Bulletin of the Geological Society of America, 100, 1720–1737.
——— (1989a) Magma chambers. Annual Reviews of Earth and Planetary Science, 17, 439–474.
——— (1989b) On convective style and vigor in sheet-like magma chambers. Journal of Petrology, 30, 479–530.
——— (1990) Reply to: Discussion of: "Crystal capture, sorting, and retention in convecting magma," by R.S.J. Sparks. Bulletin of the Geological Society of America, 102, 849–850.
——— (1991) Reply to Comments on: "On convective style and vigor in sheet-like magma chambers," by H.E. Huppert and J.S. Turner. Journal of Petrology, 32, 855–860.
Marsh, B.D., and Maxey, M.R. (1985) On the distribution and separation of crystals in convecting magma. Journal of Volcanology and Geothermal Research, 24, 95–150.
Martin, D., and Nokes, R. (1989) A fluid dynamical study of crystal settling in convecting magma. Journal of Petrology, 30, 1471–1500.
Meyer, C., Anderson, D.H., and Bradley, J.G. (1974) Ion microprobe analysis of plagioclase from "non-mare" lunar samples. Proceedings of the Lunar Science Conference, 5, 685–706.
Morse, S.A. (1992) Comment on: Partitioning of strontium between plagioclase and melt. Geochimica et Cosmochimica Acta, 56, 1735–1737.
Nagasawa, H., and Schnetzler, C.C. (1971) Partitioning of rare earth, alkali and alkaline earth elements between phenocrysts and acidic magma. Geochimica et Cosmochimica Acta, 35, 953–968.
Nelson, S.T., and Montana, A. (1992) Sieve-textured plagioclase in volcanic rocks produced by rapid decompression. American Mineralogist, 77, 1242–1249.
Nixon, G.T., and Pearce, T.H. (1987) Laser-interferometry study of oscillatory zoning in plagioclase: The record of magma mixing and phenocryst recycling in calc-alkaline magma chambers, Iztaccihuatl volcano, Mexico. American Mineralogist, 72, 1144–1162.
Oldenberg, C.M., Spera, F.J., Yuen, D.A., and Sewell, G. (1989) Dynamic mixing in magma bodies: Theory, simulations, and implications. Journal of Geophysical Research, 94, 9216–9236.
Pallister, J.S., Hoblitt, R.P., and Reyes, A.G. (1992) A basalt trigger for the 1991 eruptions of Pinatubo volcano? Nature, 356, 426–428.
Pearce, T.H., and Kolisnik, A.M. (1990) Observations of plagioclase zoning using interference imaging. Earth-Science Reviews, 29, 9–26.
Pearce, T.H., Russell, J.K., and Wolfson, I. (1987) Laser-interference and Nomarski interference imaging of zoning profiles in plagioclase phenocrysts from the May 18, 1980, eruption of Mount St. Helens, Washington. American Mineralogist, 72, 1131–1143.
Philpotts, A.R. (1990) Principles of igneous and metamorphic petrology, 498 p. Prentice Hall, Englewood Cliffs, New Jersey.
Phinney, W.C., and Morrison, D.A. (1990) Partition coefficients for calcic plagioclase: Implications for Archean anorthosites. Geochimica et Cosmochimica Acta, 54, 1639–1654.
Rutherford, M.J., and Devine, J.D. (1988) The May 18, 1980, eruption of Mount St. Helens: 3. Stability and chemistry of amphibole in the magma chamber. Journal of Geophysical Research, 93, 11949–11959.
Rutherford, M.J., and Hill, P.M. (1993) Magma ascent rates from amphibole breakdown: An experimental study applied to the 1980–1986 Mount St. Helens eruption. Journal of Geophysical Research, 98, 19667–19685.
Sato, H. (1989) Mg-Fe partitioning between plagioclase and liquid in basalts of hole 504B, ODP leg 111: A study of melting at 1 atm. Proceedings of the Ocean Drilling Program, 111, 17–26.
Schnetzler, C.C., and Philpotts, A.J. (1970) Phenocryst-matrix partition coefficients for K, Rb, Sr, and Ba with applications to anorthosite and basalt genesis. Geochimica et Cosmochimica Acta, 34, 307–322.
Shaw, H.R. (1972) Viscosities of magmatic silicate liquids, an empirical method of prediction. American Journal of Science, 272, 870–893.
Shimizu, N. (1978) Analysis of the zoned plagioclase of different magmatic environments: A preliminary ion-microprobe study. Earth and Planetary Science Letters, 39, 398–406.
——— (1983) Interface kinetics and trace element distribution between phenocryst and magma. In S.S. Augustithis, Ed., The significance of trace elements in solving petrogenetic problems and controversies, p. 175–195. Theophrastus Publishers, Athens.
Sibley, D.F., Vogel, T.A., Walker, B.M., and Byerly, G. (1976) The origin of oscillatory zoning in plagioclase: A diffusion and growth controlled model. American Journal of Science, 276, 275–284.
Singer, B.S., and Dungan, M.A. (1992) The origin of compositionally zoned Holocene magma at Volcán San Pedro, Chilean Andes. Eos, 73, 644.
Singer, B.S., Pearce, T.H., Kolisnik, A.M., and Myers, J.D. (1993) Plagioclase zoning in mid-Pleistocene lavas from the Seguam volcanic center, central Aleutian arc, Alaska. American Mineralogist, 78, 143–157.
Singer, B.S., Thompson, R.A., Dungan, M.A., Wulff, A.W., Feely, T.C., Pickens, J., Brown, L., Nelson, S.T., and Davison, J.P. (1994) 930 thousand years of volcanism at the Tatara-San Pedro Volcanic complex, Chilean Andes: A geochronologic, paleomagnetic, and geochemical record (abs.). IAVCEI meeting, Ankara, Turkey.
Smith, V.G., Tiller, W.A., and Rutter, J.W. (1955) A mathematical analysis of solute redistribution during solidification. Canadian Journal of Physics, 33, 723–745.
Sparks, R.S.J. (1990) Discussion of: "Crystal capture, sorting, and retention in convecting magma," by B.D. Marsh. Bulletin of the Geological Society of America, 102, 847–848.
Sparks, R.S.J., Huppert, H.E., and Turner, J.S. (1984) The fluid dynamics of evolving magma chambers. Philosophical Transactions of the Royal Society of London, A310, 511–534.
Sparks, R.S.J., and Marshall, L.A. (1986) Thermal and mechanical constraints on mixing between mafic and silicic magmas. Journal of Volcanology and Geothermal Research, 29, 99–124.
Sparks, R.S.J., Huppert, H.E., Koyaguchi, T., and Hallworth, M.A. (1993) Origin of modal and rhythmic layering by sedimentation in a convecting magma chamber. Nature, 361, 246–249.
Stamatelopoulou-Seymour, K., Vlassopoulos, D., Pearce, T.H., and Rice, C. (1990) The record of magma chamber processes in plagioclase phenocrysts at Thera volcano, Aegean volcanic arc, Greece. Contributions to Mineralogy and Petrology, 104, 73–84.
Steele, I.M., Hutcheon, I.D., and Smith, J.V. (1980) Ion microprobe analysis and petrogenetic interpretations of Li, Mg, Ti, K, Sr, Ba in lunar plagioclase. Proceedings of the Lunar Science Conference, 11, 571–590.
Sunagawa, I. (1992) In situ investigation of nucleation, growth, and dissolution of silicate crystals at high temperatures. Annual Reviews of Earth and Planetary Science, 20, 113–142.
Thompson, R., and Dungan, M.A. (1985) The petrology and geochemistry of the Handkerchief mesa mixed magma complex, San Juan Mountains, Colorado. Journal of Volcanology and Geothermal Research, 26, 251–274.
Tsuchiyama, A. (1985) Dissolution kinetics of plagioclase in the melt of the system diopside-albite-anorthite, and the origin of dusty plagioclase in andesites. Contributions to Mineralogy and Petrology, 89, 1–16.
Weinstein, S.A., Yuen, D.A., and Olson, P.L. (1988) Evolution of crystal settling in magma chamber convection. Earth and Planetary Science Letters, 87, 237–248.
Wilcox, R.E. (1954) Petrology of Parícutin Volcano, Mexico. U.S. Geological Survey Bulletin 965-C, 281–353.

Manuscript received July 20, 1994
Manuscript accepted April 6, 1995

## Appendix 1. Density and viscosity estimates

Temperatures (Table 1) were estimated using two pyroxene and two oxide equilibria in the San Pedro dacite and basaltic inclusion and plagioclase + magnetite oxygen isotope thermometry for the Tatara dacite. For the San Pedro dacite, Housh and Luhr's (1991) equilibria were used to estimate $H_2O$ concentrations in the melt from the composition of a coexisting (1) melt inclusion and adjacent plagioclase of $An_{47}$ and (2) matrix glass and rim plagioclase of $An_{33}$. Both estimates are about 2.0 wt% $H_2O$, consistent with the deficient totals of the microprobe analyses (Table 1; given some $Na_2O$ loss during EPMA of the inclu-

sion glass). As glass is absent from the Tatara dacite, we have adopted a value of 2.0 wt% $H_2O$ for this sample. A value of 1.0 wt% $H_2O$ was assumed for the basaltic melt that interacted with the San Pedro dacite (Table 1). Using bulk compositions and the San Pedro dacite matrix glass analysis (Table 1), with $Fe^{3+}/Fe^{2+}$ estimated following Kilinc et al. (1983) at Ni-NiO + 1 log unit $f_{O_2}$, 1 atm magma densities were calculated using Lange and Carmichael's (1987) partial molar volume data corrected for $H_2O$ following Burnham's (1979) solution model and partial molar volume data from Burnham and Davis (1971). Plagioclase densities (Table 1) were calculated as in Singer et al. (1993).

Melt viscosities assuming crystal-free liquid (Table 1) were calculated following Shaw (1972). From Marsh (1981) we have the following relation between crystal content and magma viscosity: $\mu_c = \mu_L (1-1.67X)^{-2.5}$, where $\mu_c$ is the viscosity of a crystal-rich melt in poise, $\mu_L$ is the crystal-free viscosity, and $X$ is the volume fraction of crystals in the magma. Values of $\mu_c$ were calculated using the phenocrysts modes (Table 1). The Stokes settling velocity for equant particles in a crystal-free magma is $V_s = 2\Delta\rho r^2/9\mu_L$, and Marsh and Maxey (1985) give the settling velocity in a crystal-rich magma as $V_c = V_s \{(1 - X)/(1 + X^{1/2}) e^{[5X/3(1-X/Xc)]}\}$, where $\Delta\rho$ is the crystal-melt density contrast, $r$ is the crystal radius, and $X_c$ is the critical fraction of crystals (0.60), above which the magma is essentially a rigid solid. Maximum values of $V_s$ and $V_c$ were calculated using the final crystal size of 2 mm diameter for both magmas (Table 1).